RSC Advances

PAPER

View Article Online
View Journal | View Issue

Cite this: *RSC Adv.*, 2025, **15**, 29777

Development of Cu-MOF@PVDF–PS hybrid membranes for high-temperature proton exchange membranes: electrospinning, characterization, and fuel cell performance

Enas Ahmed,[a] Ahmed A. Farghali[b] and Mai F. M. Hmamm *[a]

Received 24th May 2025
Accepted 15th July 2025

DOI: 10.1039/d5ra03667d

rsc.li/rsc-advances

Nafion membranes, while widely used in fuel cells, suffer from high cost, limited methanol resistance, and thermal instability. This study addresses these limitations by developing a Cu-MOF@PVDF–PS nanofiber membrane with enhanced proton conductivity and structural durability. The proton exchange membrane was fabricated using electrospun nanofibers derived from a polymer blend of polyvinylidene fluoride (PVDF) and polystyrene (PS). The electrospinning technique facilitated the formation of numerous tiny ionic aggregates on the membrane surface, enhancing proton conductivity. To further improve conductivity, metal–organic frameworks (MOFs) were incorporated into the polymeric membranes, enabling tunable proton conduction. In this work, a Cu(II)-based metal–organic framework (Cu-MOF) was incorporated into the PVDF–PS blend to produce hybrid membranes (Cu-MOF@PVDF–PS) with varying MOF content. The impact of different Cu-MOF loadings on the conductivity of the membrane composites was thoroughly examined. Notably, the Cu-MOF 50 wt%@PVDF–PS membrane demonstrated proton conductivity of up to 61.4 mS cm^{-1} at 353 K. The improved proton conductivity of this hybrid membrane is attributed to contributing the formation of extended range conductive network through electrospinning, followed by hot pressing, and the synergistic effects among Cu-MOF and PVDF–PS. This research paves the way for further advancements in MOF/nanofiber composite membranes for proton-conducting applications.

1. Introduction

The excessive reliance on fossil fuels has contributed to significant and irreversible environmental damage to the environment, prompting the need for sustainable and clean energy alternatives.[1,2] Fuel cells are regarded as promising options to address contemporary energy challenges. Proton exchange membrane fuel cells (PEMFCs), recognized for their superior effectiveness, power density, and environmentally friendly nature, have become a central focus of research.[3–7] Among the various electrolytes used, Nafion membranes are the most common owing to their excellent proton conductivity ($\sigma = 10^{-1}$ to 10^{-2} S cm^{-1}) at temperatures between 30 and 80 °C.[8–10] However, Nafion faces limitations, such as poor thermal stability, high production costs, and complex manufacturing processes, which hinder its large-scale practical application.[8,10,11] This has led to growing interest in alternative materials that offer improved proton conductivity, better thermal and chemical stability, and more cost-effective production methods. Despite Nafion's superior proton conductivity under hydrated conditions, its limitations such as high cost, limited thermal and mechanical stability at elevated temperatures, and significant methanol crossover restrict its broader application in fuel cells, particularly in direct methanol fuel cells (DMFCs). To address these issues, a blend of polyvinylidene fluoride (PVDF) and polystyrene (PS) was selected for membrane fabrication. PVDF offers excellent thermal and chemical stability, while PS contributes rigidity, processability, and compatibility with functional modifications. The PVDF/PS composite structure provides a cost-effective, mechanically robust, and chemically resistant matrix, which can outperform Nafion in harsh operating environments, especially when combined with proton-conductive fillers such as metal–organic frameworks (MOFs). The combination of polyvinylidene fluoride (PVDF) and polystyrene (PS) was chosen to take advantage of their complementary properties. PVDF is known for its excellent thermal stability, chemical resistance, and mechanical strength, while PS offers good film-forming ability, ease of processing, and compatibility with sulfonation or other functionalization. Blending these polymers enables the formation of flexible, robust nanofiber membranes with enhanced

---

[a] *Renewable Energy Science and Engineering Department, Faculty of Postgraduate Studies for Advanced Science, Beni-Suef University, 62511 Beni-Suef, Egypt. E-mail: mai.farg@psas.bsu.edu.eg; mai_farge@yahoo.com*

[b] *Materials Science and Nanotechnology Department, Faculty of Postgraduate Studies for Advanced Sciences (PSAS), Beni-Suef University, 62511 Beni-Suef, Egypt*

mechanical integrity and tunable properties suitable for proton exchange applications. Metal–organic frameworks (MOFs) have attracted significant regard as promising proton-conducting materials owing to their high porosity, tunable structures, and versatility. Numerous MOFs have been synthesized, showing potential for high-temperature applications.[12–14] For example, Yang *et al.* developed a chemically stable and structurally versatile MOF, BUT-8(Cr)A, with sulfonic acid sites that exhibited high proton conductivity of 1.27×10^{-1} S cm^{-1} at 80 °C and 100% relative humidity.[15] Similarly, Wang *et al.* reported a Pb-based MOF with strong anisotropic conductivity,[16] and Zou *et al.* demonstrated a modified UiO-66 MOF with enhanced proton conductivity.[17] Despite these advances, the poor film-forming properties of many MOFs limit their direct application in proton exchange membranes (PEMs).

To overcome this, hybrid membranes combining MOFs with functional organic polymers have shown promise in improving the stability and performance of PEMs.[18–22] Electrospinning, a simple method for producing homogeneous nanofiber membranes, has been explored to create nanostructured PEMs with high proton conductivity. The electrospinning process promotes the formation of dense ionic clusters along the fibers, providing long-distance proton conducting channels.[23] The extensive surface area of the nanofibers allows for the efficient doping of proton donors, enhancing the overall proton conductivity. While several electrospun proton-conductive polymers have been reported,[24–26] the creation of mixed matrix membranes (MMMs) for PEM applications remains limited.

In this study, we present the fabrication of proton exchange membranes using a blend of polyvinylidene fluoride (PVDF) and polystyrene (PS) through electrospinning. PVDF is a durable and thermally stable polymer, but its lack of active functional groups limits its application as a PEM. Conversely, PS-based proton exchange resins, which are easily thermoformed and soluble in water, offer an ideal alternative. Given China's position as the largest producer of ion exchange resins,[27] we propose a cost-effective approach for manufacturing PVDF/PS-based PEMs embedded with Cu MOF. The incorporation of copper-based MOFs (Cu MOFs) is particularly promising due to their potential for enhancing the electrochemical properties and catalytic activity of fuel cells. Cu MOFs, recognized for their large surface area and tunable porosity, offer improved charge transport and efficiency, making them ideal for enhancing fuel cell performance.

This paper aims to explore the impact of Cu MOF concentration, the ratio of PVDF to PS, and electrospinning parameters regarding the performance of the proton exchange membranes. Specifically, we investigate the impact of these factors on proton conductivity and the overall performance of PEMs for fuel cell applications.

2. Materials and methods

2.1. Materials

Polystyrene (pellets), poly vinylidene fluoride (powder), *N*,*N* dimethylformamide (99%) and methanol (HPLC) were acquired from (Alfa Aesar). Terephthalic acid ($C_8H_6O_4$, benzene – 1,4 dicarboxylic acid) pure, 98%, SRL and copper II nitrate ($Cu(NO_3)_2 \cdot 3H_2O$) were purchased from Alpha Chemik.

2.2. Preparation of Cu-metal–organic frame works

Teflon-lined stainless-steel jar was filled with a mixture of $Cu(NO_3)_2 \cdot 3H_2O$ (0.1052 g), terephthalic acid (0.130 g), and H_2O (45 mL). Following a 72 hours heating period at 120 °C, the reaction was gradually reduced to room temperature, yielding light green-blue crystals that were then thoroughly cleaned three times using deionized water.

2.3. Solution preparation

A factorial experiment was conducted to examine the impact of operational parameters, such as polymer concentration, applied voltage, and feed rate of the polymer solution, on the average fiber diameter, which influences the morphology of the poly(vinylidene fluoride) (PVDF)–polystyrene (PS) nanofiber membranes.

Solutions of PVDF–PS were prepared at concentrations of 10, 15, 20, and 30 wt% in *N*,*N*-dimethylformamide (DMF). The solution was heated to 60 °C and stirred for 1 hour, then left to stir at room temperature overnight. The resulting solution was loaded into a 10 mL syringe with a stainless-steel needle. A capillary needle with an inner diameter of 0.6 mm was connected to the positive terminal of a high voltage power supply, while the syringe was mounted on a syringe pump to achieve the optimal concentration for the nanofiber membrane.

The PVDF–PS solution was then electrospun at voltages between 25 kV and 20 kV, with flow rates varying from 0.5 mL h^{-1} to 1.5 mL h^{-1}, and a constant syringe-to-collector distance of 14 cm. Then PVDF–PS is employed to formulate the solution at concentration 10 wt% in *N*,*N*-dimethylformamide (DMF) with different ratio PVDF : PS (10 : 90, 20 : 80, 30 : 70, 40 : 60, 50 : 50, 60 : 40, 70 : 30, 80 : 20 and 90 : 10) respectively the preparation method shown in Fig. 1. Following the electrospinning procedure, the membranes were subjected to a 10 minutes hot press at 100 °C. The items had the designation PVDF–PS nanofiber membrane. Finally, preparation of nanofiber proton exchange membranes blended with different ratio of (5, 10, 20, 30, 40 and 50%) Cu MOF using electrospinning technique as shown in Fig. 2.

2.4. Optimization of the electro spinning parameters affected membrane performance

The objective of this study is to improve the fiber formation process by modifying three crucial parameters: the polymer blend solution concentration, the applied voltage, and the solution flow rate. The distance from the tip to the collector is maintained constant throughout the experiment. Electrospinning is used for optimization, with each of the parameters being tested at three different levels. The specific amounts of the parameters used are presented in Table 1.

An optical microscope was used to measure the mean diameters of the beads and fibers. A total of 100 fiber measurement points were randomly selected to ensure that the sample represents all regions.

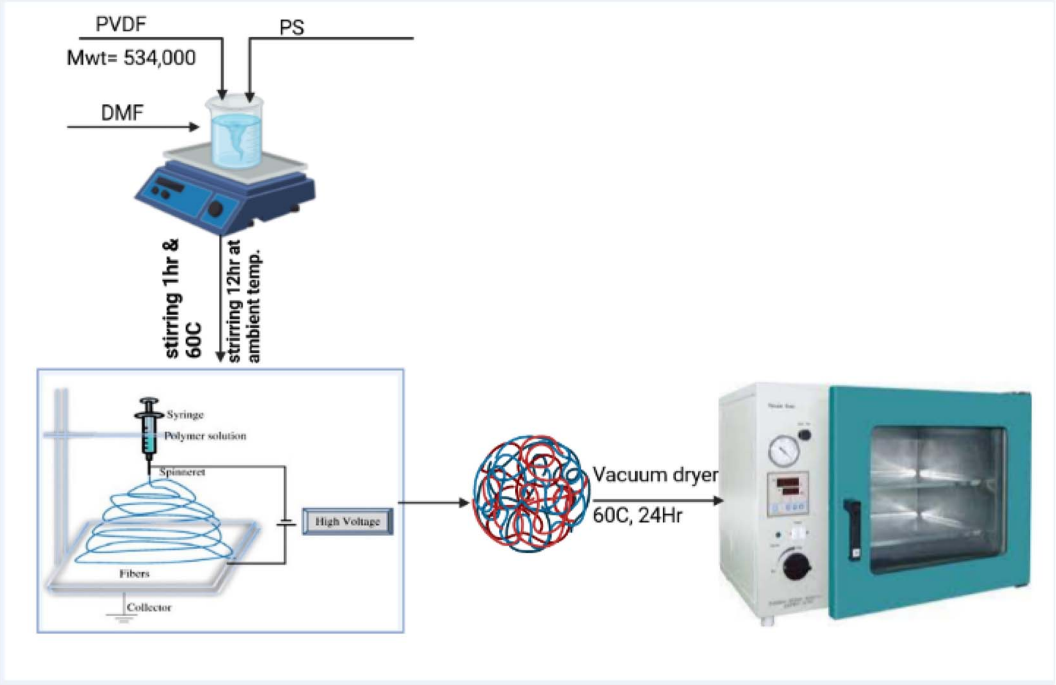

Fig. 1 The preparation method for nano-fiber membranes.

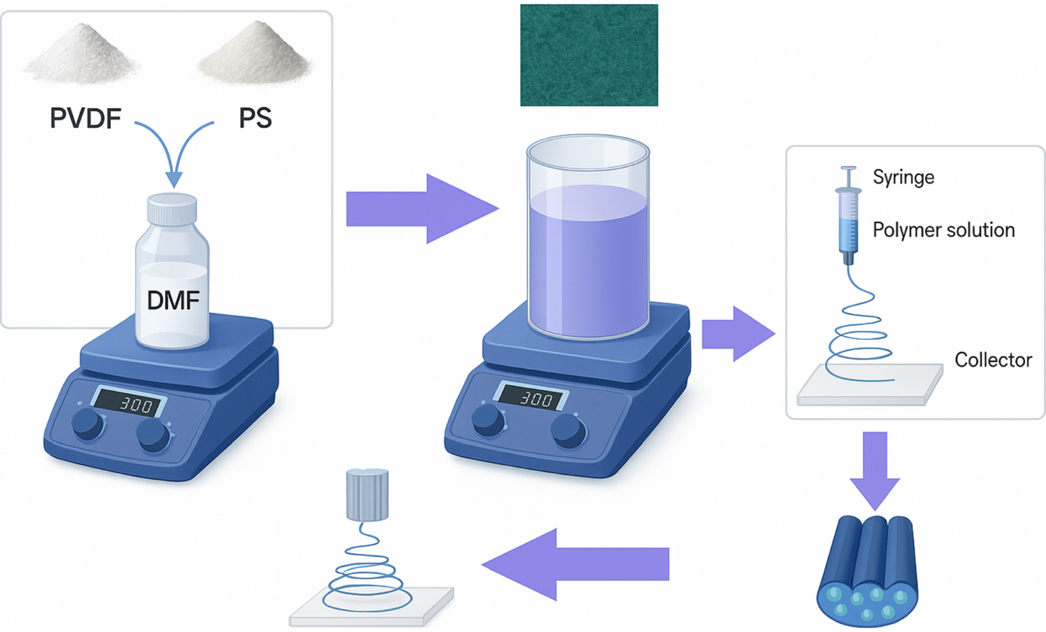

Fig. 2 The preparation method of PVDF–PS nano fiber doped with Cu MOF.

2.5. Ion exchange capacity

The ion exchange capacity (IEC) of the membranes was measured through the acid–base titration technique. A dry, pre-weighed membrane was submerged in 20 milliliters of a 1 M sodium chloride solution for 24 hours, allowing H^+ ions to be replaced by Na^+ ions (Abdel-Hady *et al.* 2018 [40]). Afterward, the solution containing the released protons was titrated with a standardized NaOH solution (0.01 mol L^{-1}), using phenolphthalein as the indicator. The IEC value for the membrane was then determined using the following formula:

$$\mathrm{IEC} = \frac{V_{\mathrm{NaOH}} \times C_{\mathrm{NaOH}}}{W_{\mathrm{dry}}} \times 100\% \tag{1}$$

In this equation, IEC refers to the ion exchange capacity (meq g^{-1}), V_{NaOH} is the volume of the NaOH solution used,

Table 1 Electrospinning parameters used for the fabrication of PVDF–PS membranes without Cu-MOF. The table lists the concentrations of the polymer solution (in wt%), the corresponding voltage and flow rate conditions applied during membrane preparation

Variables			
Concentration (wt%)			
10 wt%	15 wt%	20 wt%	30 wt%
Voltage (kV)			
25	20	15	
Flow rate (mL h^{-1})			
1.5	1	0.5	

C_{NaOH} is the molarity of the NaOH solution, and W_{dry} represents the mass of the dry sample.

2.6. Water uptake (%), methanol uptake (%) and swelling ratio (%)

The water uptake (WU) and swelling ratio (SR) were determined by observing the variations in weight and area before and after the hydration process. All membranes were dried in a vacuum at 80 °C until their weight remained constant. Subsequently, the weights and areas of the samples were documented as W_{dry} and A_{dry}, respectively. These membranes were then immersed in deionized water at room temperature for 24 hours, the surface water was then removed using filter paper, the weights and areas of the samples were recorded. These were noted as W_{wet} and A_{wet}, respectively. The water uptake (WU) and swelling ratio (SR) were then calculated using the following formulas:

$$\mathrm{WU} = \frac{W_{\mathrm{wet}} - W_{\mathrm{dry}}}{W_{\mathrm{dry}}} \times 100\% \tag{2}$$

$$\mathrm{SR} = \frac{A_{\mathrm{wet}} - A_{\mathrm{dry}}}{A_{\mathrm{dry}}} \times 100\% \tag{3}$$

methanol uptake (%) was evaluated using the same procedure as water uptake (%), with methanol substituted for water.

2.7. FT-IR spectra, SEM-EDX, X-ray diffraction (XRD), contact angle and TGA measurements

The FTIR spectra (400–4000 cm^{-1}) were recorded with Vertex-70 (Bruker 1341, Germany). The morphology of surfaces and cross-section of nanocomposites were investigated by using a Scanning electron microscopy (STEM) (ZEISS), combined with energy dispersive X-ray (EDAX) and mapping spectroscopy. Samples under investigation XRD was employed to assess the crystallinity of the prepared nanocomposites using a PANalytical X-ray diffractometer (Netherlands). The diffractometer is equipped with a Cu Kα radiation source, a wavelength of 1.54 Å, an accelerating voltage of 40 kV, and a current of 35 mA. Water contact angle (WCA) measurement was performed on p/n 100-25-A Automated Tilting Base. A 5 mL droplet of deionized water was applied for testing at three different spots on each sample and left for 10 seconds to ensure complete wetting. Thermogravimetry analysis (TGA) of the nanocomposites were carried out using SENSYS evo TG-DSC under N_2 gas flow, at the heating rate of 10 °C min^{-1} in nitrogen atmosphere from 25 to 800 °C.

2.8. Proton conductivity

The proton conductivity of the membranes was analyzed using the AC impedance method within a temperature range of 20 °C to 80 °C. The electrochemical impedance spectroscopy (EIS) technique was employed with a HIOKI-LCR (3532) phase analyzer, operating over a frequency range of 50 Hz to 5 MHz and using a 500 mV oscillating voltage in the conductivity cell. The proton conductivity, σ (S cm^{-1}), was then calculated using the following formulas:

$$\sigma = \frac{L}{RA} \tag{4}$$

where L (cm) represents the distance between the two electrodes, A (cm^2) is the cross-sectional area of the membrane sample, and R (Ω) is the measured resistance of the membrane. The activation energy (E_a) of the membrane sample was determined from the conductivity data (σ) within the temperature range of 20 °C to 80 °C using the Arrhenius equation:

$$\ln \sigma = \ln A - \frac{E_a}{k_B T} \tag{5}$$

where A is the frequency pre-factor, k_B is the Boltzmann constant, and T (K) represents the absolute temperature.

3. Results and discussion

3.1. Morphology of fiber mats and membranes

The electrospinning method utilizes a high voltage to charge the surface of a polymer solution droplet, causing the formation of a liquid jet that is ejected through a spinneret.

The jet undergoes continuous stretching due to bending instability, forming continuous, ultra-thin strands. Consequently, the electrospinning method has been used to create a large number of functional nanofibers. It is important to highlight that a polymer-based sol–gel can be electrospun to create inorganic nanofibers. Electrospun PVDF–PS were successfully synthesized by electrospinning technique at different voltages, different flow rate and polymer solution concentration. The morphological characters demonstrated clearly indicate that PVDF–PS fibers possessed remarkable spinning ability.

Fig. 3–6 display scanning electron microscopy (SEM) images of PVDF–PS nanofiber mats fabricated *via* electrospinning using different total polymer concentrations: 10, 15, 20, and 30 wt%, respectively. At 10 wt%, the electrospun fibers exhibited excellent morphology, forming a consistent, bead-free network with uniform diameters (Fig. 3). Fig. 3A presents a low-magnification view of the smooth, continuous fiber formation, while Fig. 3B provides a closer look, confirming the homogeneity in surface texture and diameter distribution. Attempts to electrospin polymer solutions with concentrations below 10 wt% were unsuccessful, as only droplets were observed instead of fibers,

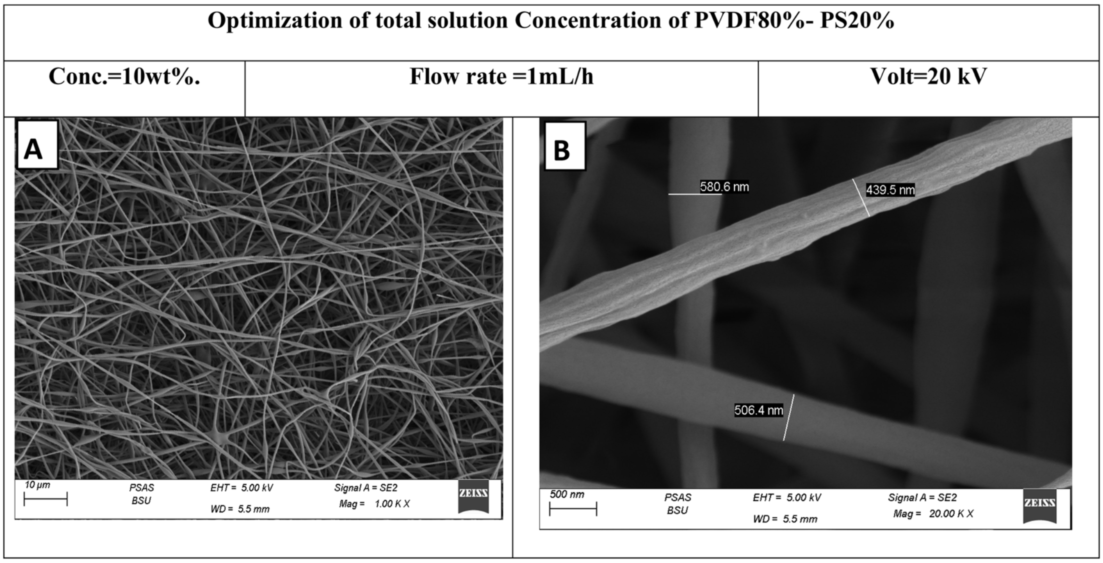

Fig. 3 SEM images of PVDF–PS nanofibers electrospun at 10 wt% total polymer concentration. (A) Low-magnification image showing uniform, continuous fibers without bead formation. (B) Higher magnification revealing smooth surface morphology and consistent diameter distribution.

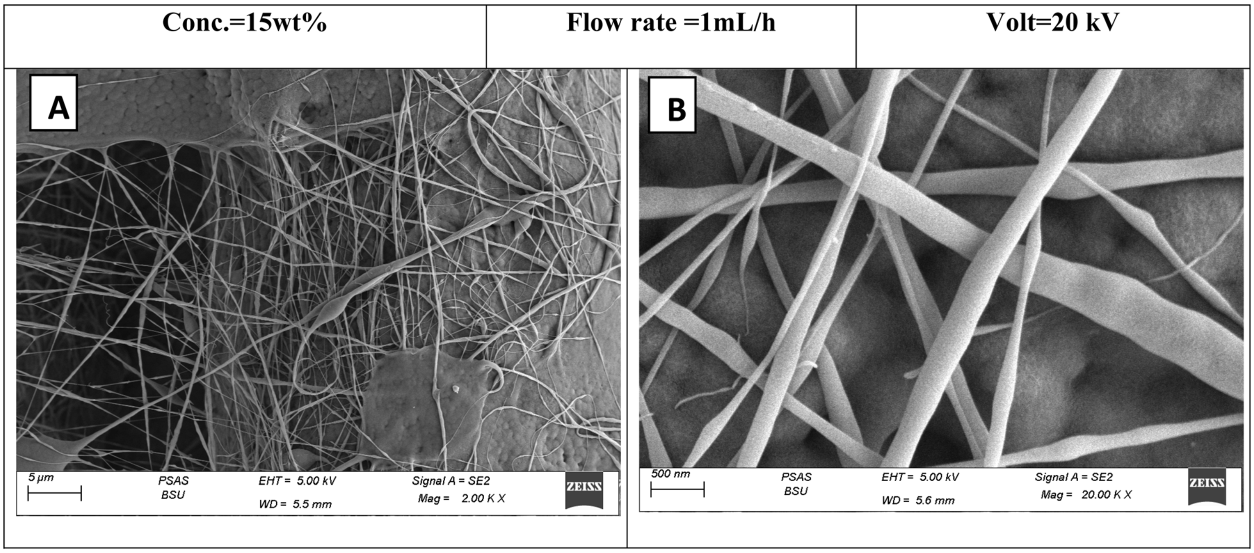

Fig. 4 SEM images of PVDF–PS nanofibers electrospun at 15 wt% total polymer concentration. (A) Fiber network with intermittent droplet formation indicating partial instability in spinning. (B) Close-up image highlighting variation in fiber thickness and onset of bead formation.

indicating that the solution lacked sufficient viscosity and chain entanglement for stable jet formation.

Increasing the polymer concentration to 15 wt% led to a decrease in fiber regularity, as seen in Fig. 4. Fig. 4A shows a partially stable fiber network with occasional droplets, while Fig. 4B captures thickness variations and signs of early bead formation, indicating a moderate level of solution instability. Further increasing the concentration to 20 wt% resulted in more pronounced morphological defects (Fig. 5). Fig. 5A reveals irregular fiber structures with noticeable droplet formation on the surface, and Fig. 5B highlights disrupted uniformity and hints of phase separation under high magnification. At 30 wt% (Fig. 6), the fibers appeared coarser and less uniform due to the high solution viscosity. Fig. 6A illustrates a dense, uneven fiber network with minor bead formation, and Fig. 6B shows localized thickening and partial fiber merging, likely caused by limited jet stability during spinning. Overall, the optimal electrospinning condition for producing uniform PVDF–PS nanofibers was achieved at 10 wt%, while both lower and higher concentrations led to instability—either by failing to form fibers or producing non-uniform structures due to insufficient molecular entanglement or excessive viscosity.

In this work, the electrospinning procedure used to create PVDF–PS nanofibers has been attempted, and the parametric influence on the electrospinning process was systematically analyzed. The influence of three key parameters high voltage,

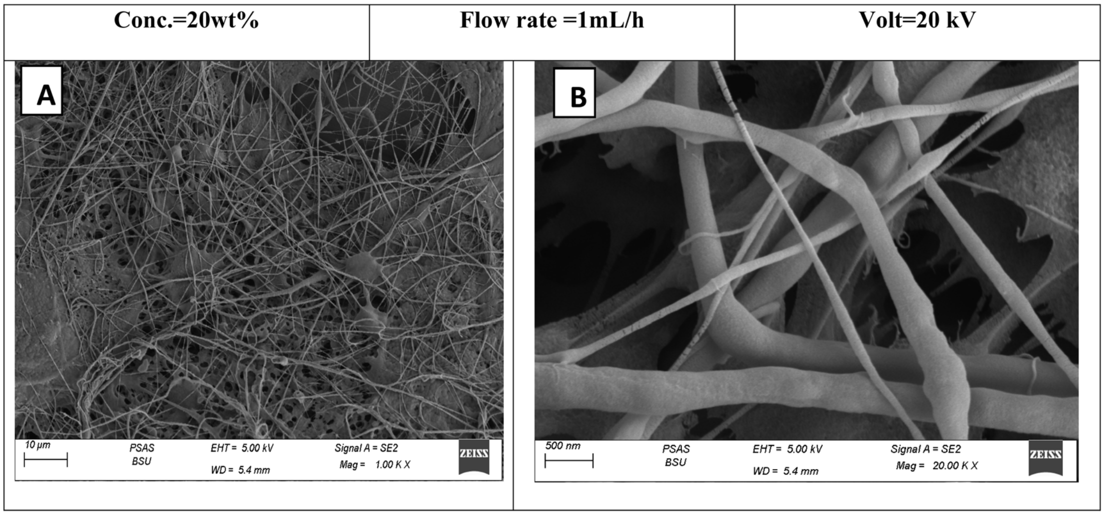

Fig. 5 SEM images of PVDF–PS nanofibers electrospun at 20 wt% total polymer concentration. (A) Fiber structure with increased irregularity and droplet-like formations on the surface. (B) High magnification showing reduced fiber uniformity and minor phase separation.

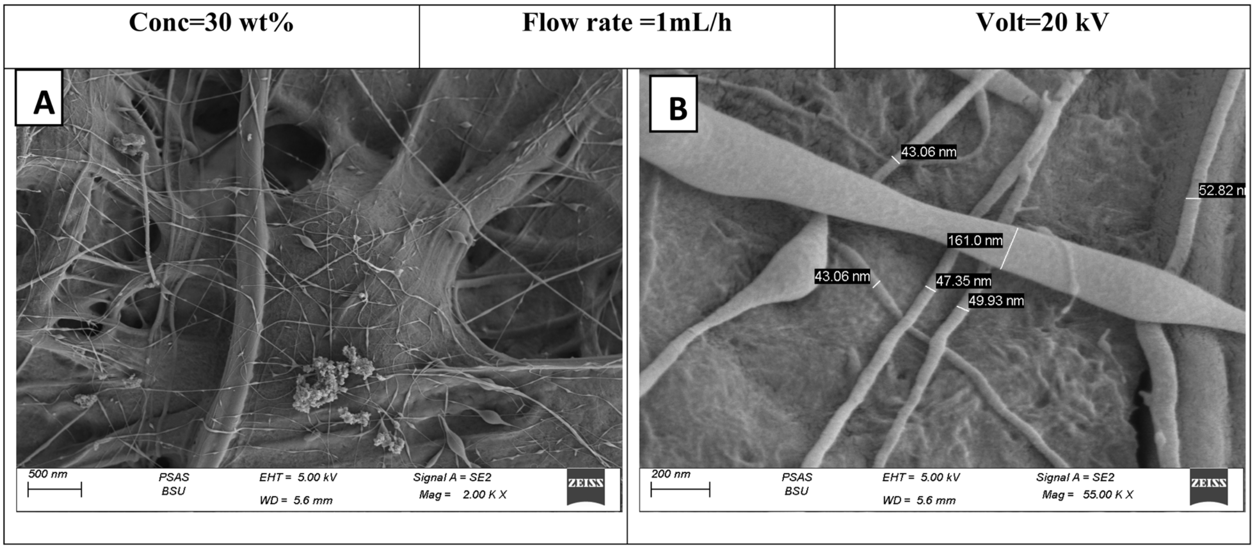

Fig. 6 SEM images of PVDF–PS nanofibers electrospun at 30 wt% total polymer concentration. (A) Morphology revealing dense network with non-uniform diameters and minor bead presence. (B) Detailed view of thickened fibers and partial fusion due to higher solution viscosity.

polymer concentration, and flow rate of the polymer solution was examined. The results revealed that the electrospun PVDF–PS fibers produced had diameters ranging from 510 nm. From the data shown in Fig. 7 and 8 the optimum condition to obtain PVDF–PS nanofibers flow rate $= 1$ mL h^{-1} from Fig. 8 where below 1 mL h^{-1} no fiber was obtained just droplet, high voltage $= 20$ kV from Fig. 9 and 10 high voltage mean fiber with good (thin, homogenous) diameter so we start from 20 kV where below no fiber was obtained just droplet and polymer solution concentration (10 wt%). The optimal fiber diameter was primarily influenced by two key design variables: polymer concentration and applied voltage, as both had a notable impact on the fiber morphology. In contrast, the flow rate had the least effect compared to the other two factors.

3.2. Optimization of PVDF–PS content blend nano fiber membranes

The surface morphology and structural uniformity of PVDF–PS nanofibers synthesized with varying polymer blend ratios were systematically analyzed using scanning electron microscopy (SEM), as illustrated in Fig. 11–17. The nanofibers prepared with a PVDF : PS ratio of 80 : 20 exhibited considerable bead formation and irregularity, suggesting suboptimal spinnability and unstable jet behavior during electrospinning (Fig. 15A and B). In contrast, blends with higher PS content, specifically 10 : 90, 40 : 60, 50 : 50, and 60 : 40, resulted in more uniform, defect-free nanofibers with well-aligned orientations. At a 10 : 90 ratio (Fig. 11), the fibers appeared fine and aligned at low magnification (A), with higher magnification images (B) revealing

Conc=10wt%	Flow rate =1.5 mL/h	Volt=20 kV
	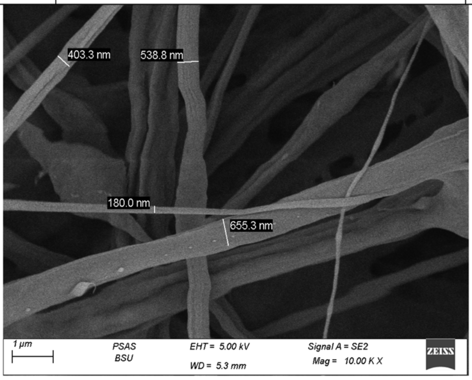	

Fig. 7 SEM images for flow rate (1.5 mL h^{-1}).

Conc.=10wt%	Flow rate =1 mL/h	Volt=20 kV
	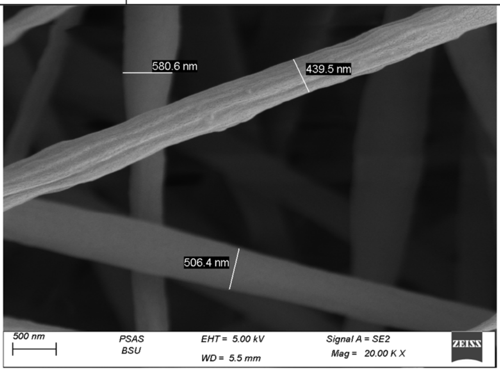	

Fig. 8 SEM images for flow rate (1 mL h^{-1}).

Optimization of High Voltage for PS20%-PVDF80%		
Conc.=10wt%	Flow rate =1 mL/h	Volt=25kV
	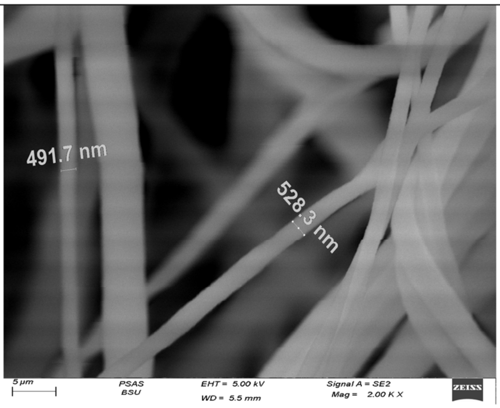	

Fig. 9 SEM images for high voltage (25 kV).

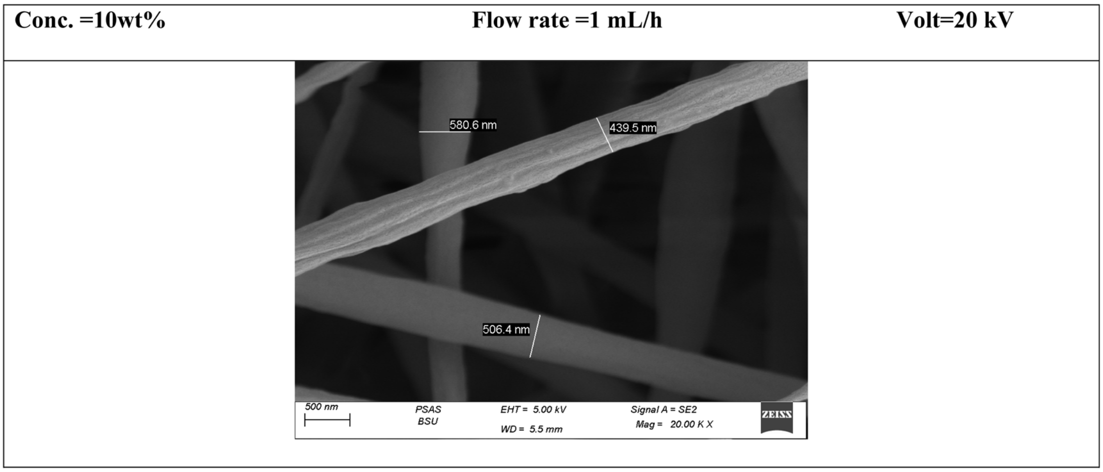

Fig. 10 SEM images for high voltage (20 kV).

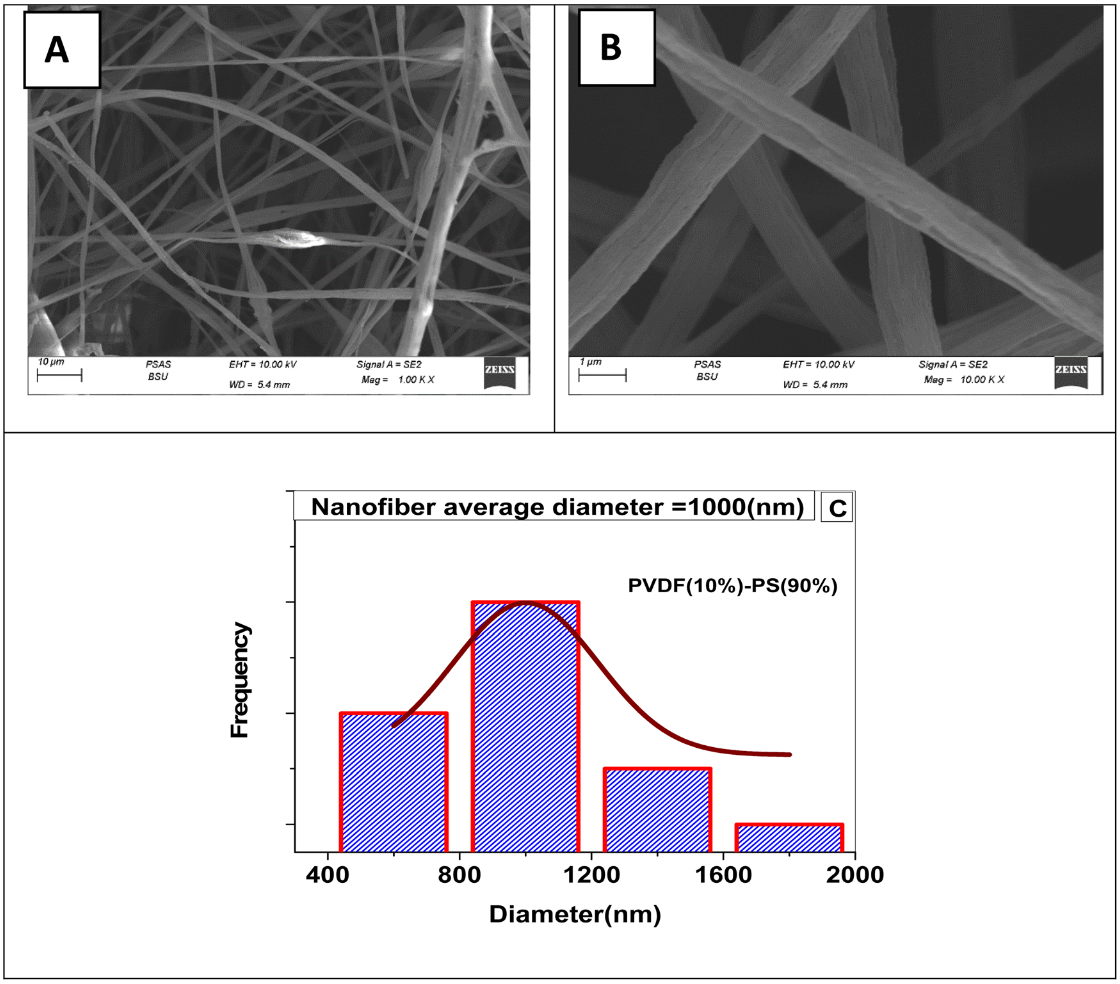

Fig. 11 SEM micrographs of PVDF : PS nanofibers at a 10 : 90 blend ratio. (A) Low-magnification image showing thin, well-aligned fibers with minimal structural defects. (B) High-magnification view highlighting smooth surface morphology and consistent fiber thickness. (C) Histogram showing narrow fiber diameter distribution.

smooth surfaces and minimal diameter variation. The fiber diameter distribution is presented in histogram form in (C). Similarly, the 40 : 60 PVDF : PS composition (Fig. 12) yielded continuous, bead-free fibers, as seen in both the low (A) and high magnification views (B), with narrow diameter spread illustrated in (C). Nanofibers produced from the 50 : 50 blend

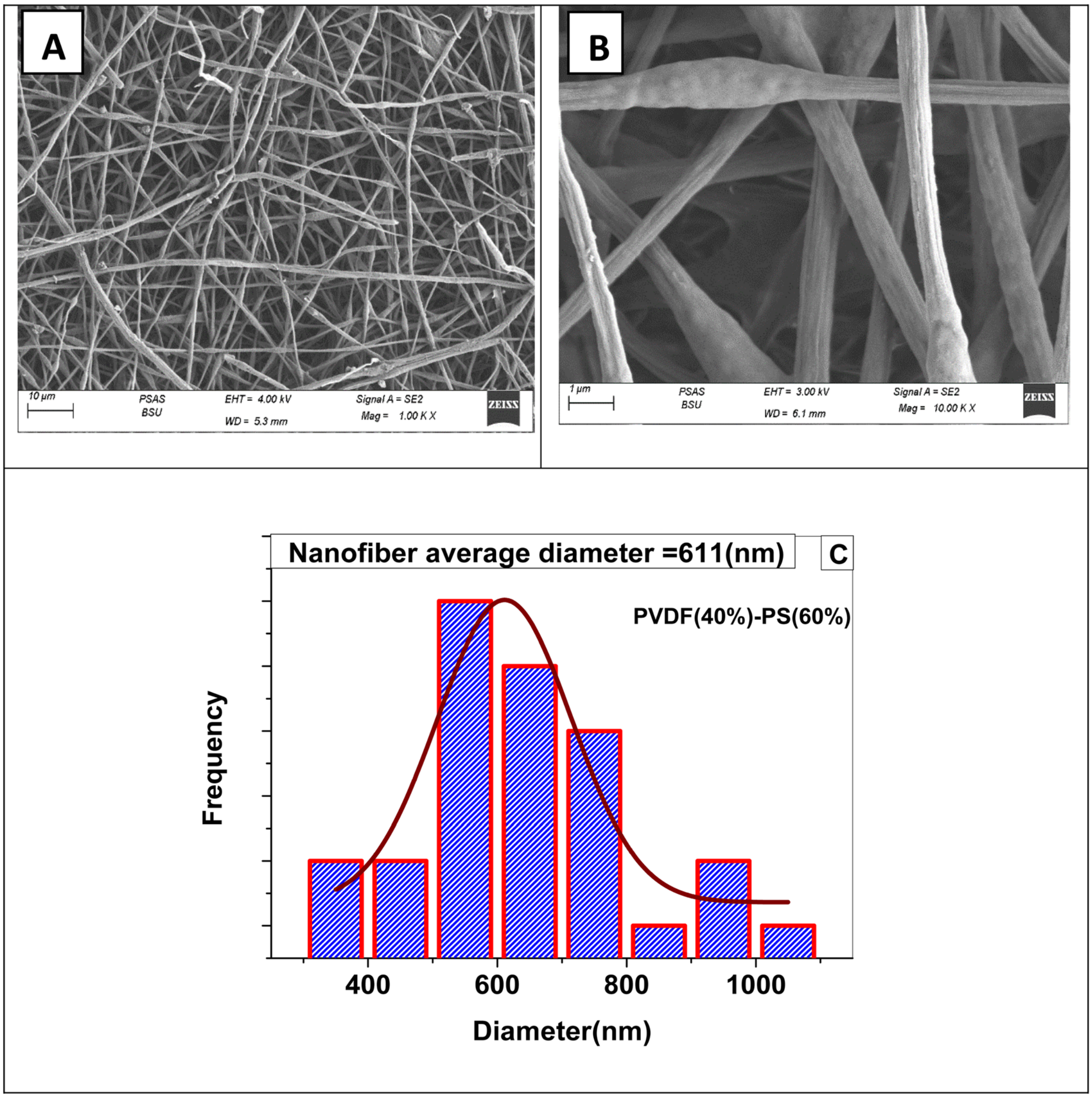

Fig. 12 SEM images of PVDF : PS nanofibers fabricated with a 40 : 60 blend ratio. (A) Uniform fiber network observed at low magnification. (B) High-resolution view confirming the absence of beads and homogeneous fiber formation. (C) Diameter distribution profile demonstrating improved size consistency.

(Fig. 13) demonstrated consistent morphology and diameter distribution, with (A) and (B) confirming structural uniformity and (C) providing quantitative support through diameter analysis. The 60 : 40 composition (Fig. 14) resulted in densely packed fibers with excellent uniformity and the smallest average diameter recorded across all tested ratios, as evidenced by images (A and B) and the distribution profile in (C). Quantitative analysis revealed a notable reduction in average fiber diameter with increasing PVDF content, particularly up to the 60% threshold, where the diameter decreased from around 1000 nm to approximately 124 nm. This improvement is likely due to enhanced solution viscosity and better chain entanglement, which contribute to stable fiber jet formation during electrospinning.

To improve the mechanical cohesion of the nanofibrous structure, selected membranes underwent thermal compression. SEM micrographs of the hot-pressed 50 : 50 membrane (Fig. 16) showed that the fibrous morphology remained intact post-processing (A), with no visible pore collapse observed in the high-resolution image (B), indicating improved membrane compactness. Finally, the relationship between fiber diameter and PVDF content is summarized in Fig. 17. The data highlight a continuous decline in diameter with increased PVDF concentration, reaching an optimal range at 60 : 40. This composition demonstrated a favorable balance between structural regularity, reduced fiber size, and membrane robustness—making it the most suitable formulation for potential proton exchange membrane (PEM) applications.

3.3. Thermogravimetry (TGA) analysis

The TGA results for pure PVDF, PS, and the composite materials are presented in Fig. 18. The onset temperatures of PVDF, PS, PVDF–PS, Cu MOF@PVDF–PS are respectively 453 °C, 358 °C, 374 °C and 305 °C, showing that PVDF has a greater thermal

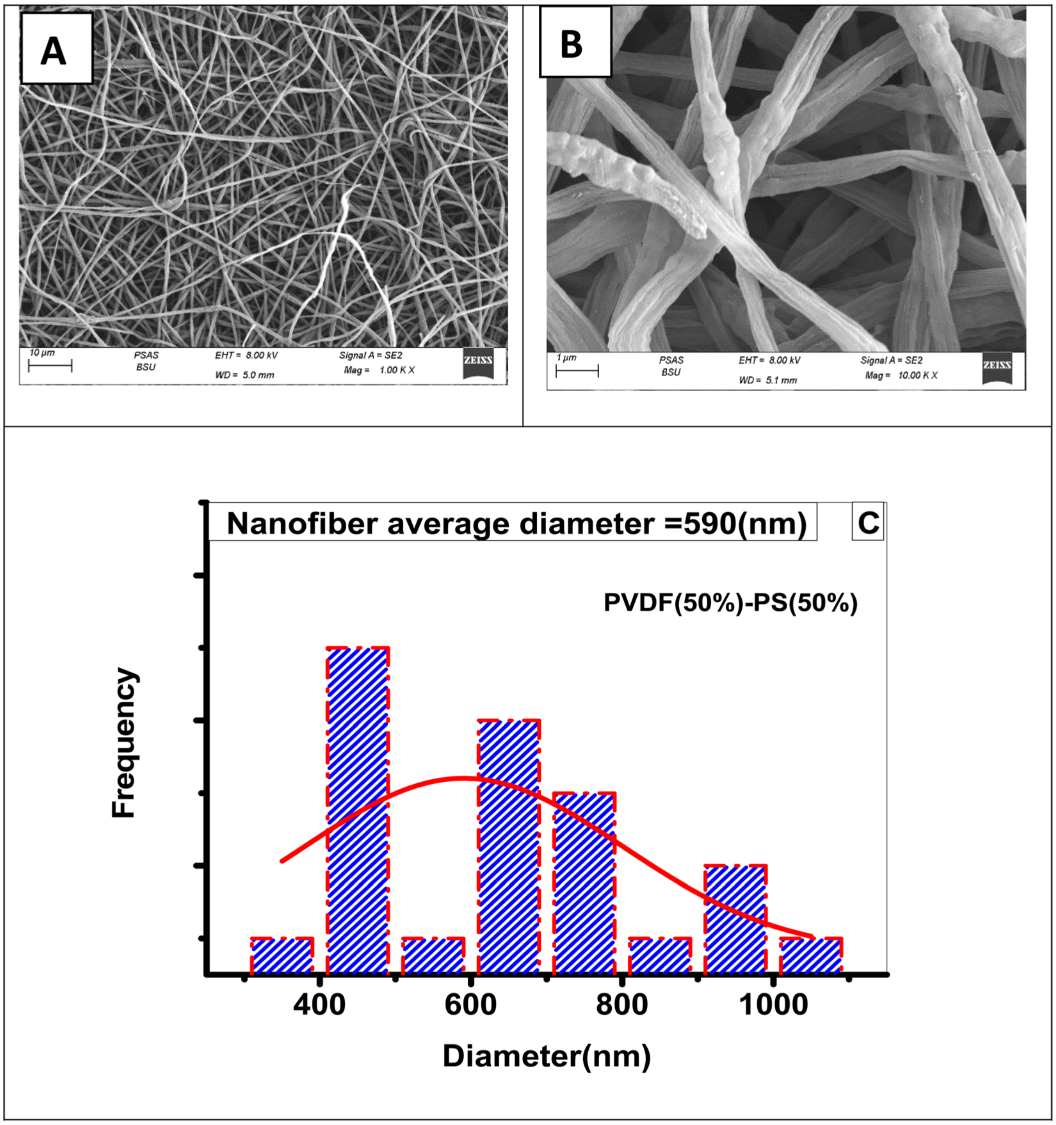

Fig. 13 SEM characterization of nanofibers from a 50 : 50 PVDF : PS blend. (A) Overview image illustrating regular fiber alignment. (B) Close-up view showing fiber continuity and uniform diameters. (C) Fiber diameter distribution indicating narrow variation.

stability and that very little water evaporated throughout this process. The individual deterioration of PS and PVDF is the cause of the two-step weight loss of the PVDF–PS mixture, corresponding to the weight fractions of PS and PVDF, respectively, shows that the thermal stability of PS is improved by the inclusion of PVDF in the composite. Regarding the addition of Cu MOF nanoparticles, Fig. 18 shows that the composites exhibit lower thermal stability compared to the PVDF–PS blend. The slight decrease in thermal stability observed in the Cu-MOF/PVDF–PS composite, as compared to the pristine PVDF–PS membrane, can be explained by several factors. First, Cu-MOF particles often contain coordinated water and organic ligands that may decompose at lower temperatures, creating localized degradation zones within the polymer matrix. Second, the presence of rigid MOF crystals disrupts the regular packing of polymer chains, reducing the overall crystallinity of PVDF–PS and lowering its decomposition threshold. Lastly, during heating, MOF particles can catalyze degradation pathways or generate acidic by-products, which further accelerate polymer breakdown. These combined effects lead to the observed decrease in thermal stability. Although the composites are thermally stable above 305 °C. The Cu MOF@PVDF–PS composite membranes begin to degrade at 323 °C, according to the TGA data. This shows that these sample membranes can satisfy the demands of PEMs operating at high temperatures, where the working conditions are always in a range of 80–200 °C.[28]

3.4. FT-IR analysis

The main chemical bonds observed in Fig. 19 for pure PS electrospun membranes are as follows: the peak at 3025 cm^{-1} is associated with aromatic C–H stretching, the sharp peak at 2921 cm^{-1} corresponds to asymmetric CH_2 stretching, and the

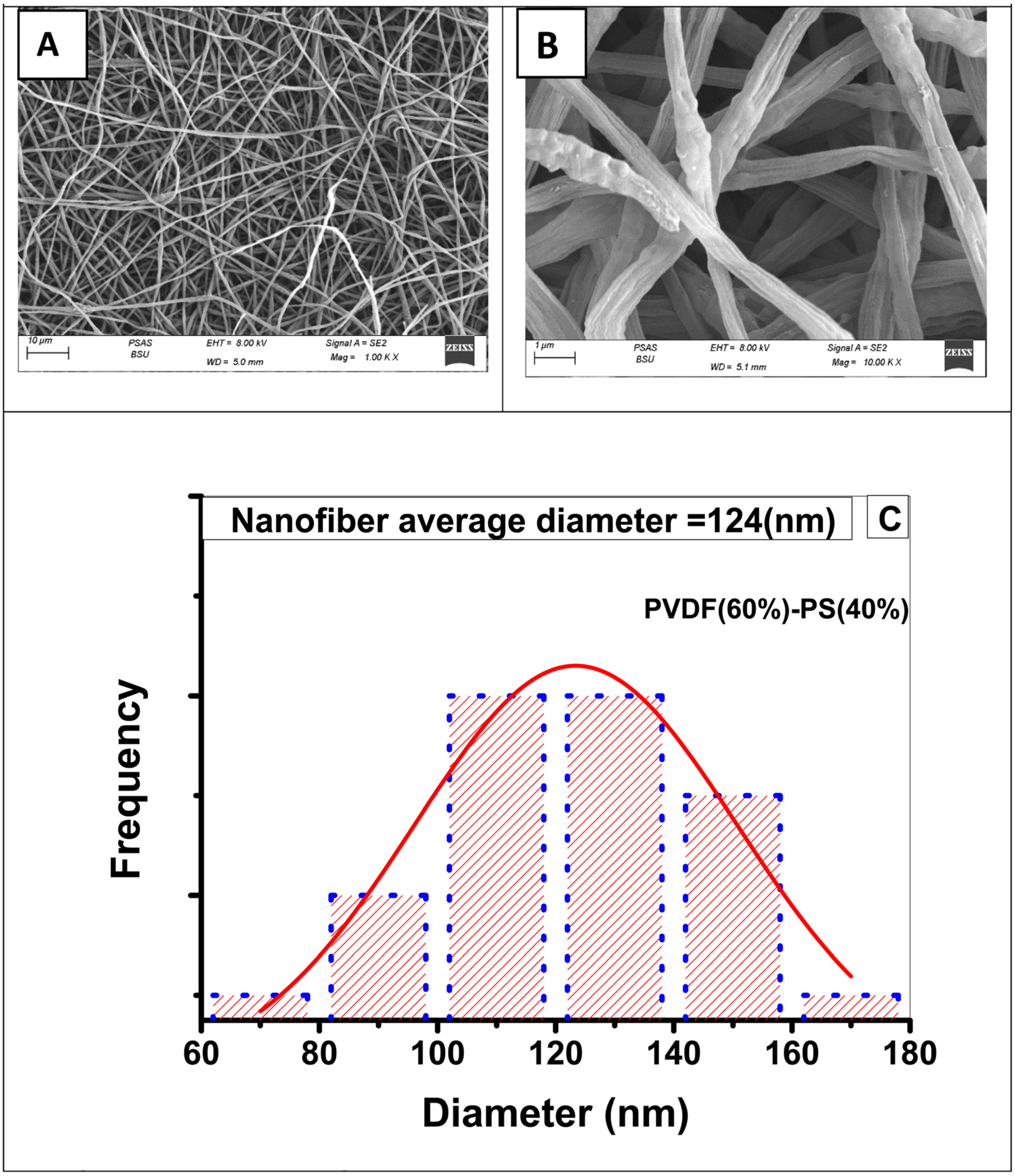

Fig. 14 SEM analysis of PVDF : PS nanofibers at a 60 : 40 ratio. (A) Dense and interconnected fiber network under low magnification. (B) High-magnification image showing highly uniform, bead-free nanofibers. (C) Histogram indicating the smallest average fiber diameter among all blends.

peaks at 1492 cm^{-1} and 1451 cm^{-1} are attributed to aromatic C═C stretching.[29] The FTIR of pure PVDF membranes was shown in Fig. 19. The absorption peaks at 488, 610, 761, and 976 cm^{-1} are characteristic of the α-crystal form. Fig. 19 displays the FTIR spectrum of the pure PVDF membrane. The peaks at 3025, 1405, and 1195 cm^{-1} are attributed to the stretching and deformation vibrations of CH_2 and the CF_2 stretching vibration, respectively.[30] It can also be obtained from Fig. 19 that most absorption peaks of PVDF and PS reversed in blended PVDF–PS membrane.

FT-IR is a powerful analytical method used to confirm the synthesis of Cu MOF. Fig. 20 presents the FT-IR spectra of the Cu metal–organic framework. The Cu-MOF exhibits peaks at 1569.9 and 1398 cm^{-1}, corresponding to the asymmetric and symmetric stretching modes of the coordinated carboxylic acid, respectively.[31,32] The peaks at 1020 and 734 cm^{-1} are attributed to the δ(C–H) and γ(C–H) vibrations of the aromatic rings, respectively. This suggests that the aromatic ring is present, confirming the inclusion of the organic ligand in the final product. Additionally, the bands at 1508 and 775.33 cm^{-1} correspond to the vibrations of the phenyl ring.[32] The broad

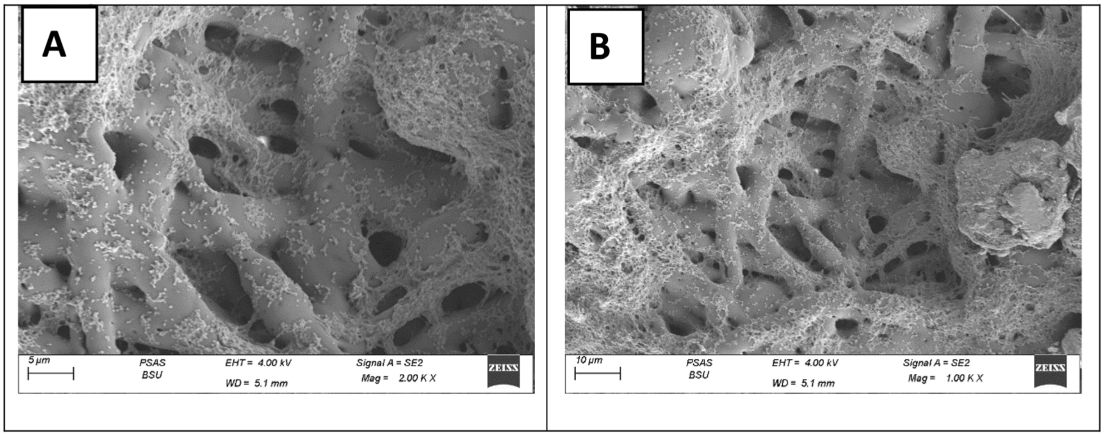

Fig. 15 SEM images of PVDF : PS nanofibers at an 80 : 20 blend ratio. (A) Low-magnification view revealing irregular fiber formation with frequent bead defects. (B) High-magnification image emphasizing poor morphology and structural discontinuity.

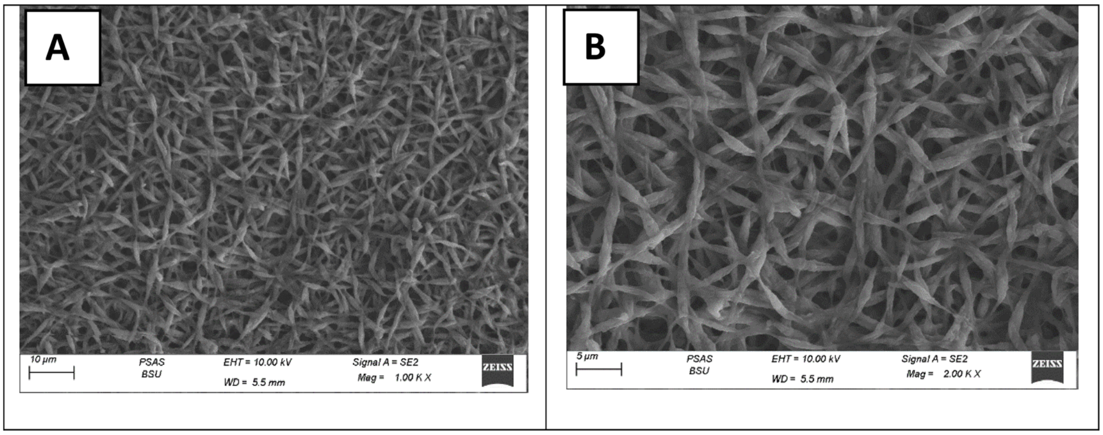

Fig. 16 SEM images of the 50 : 50 PVDF : PS nanofiber membrane after hot pressing. (A) Compressed fiber network preserving the original morphology. (B) High-resolution view showing dense fiber packing without pore collapse.

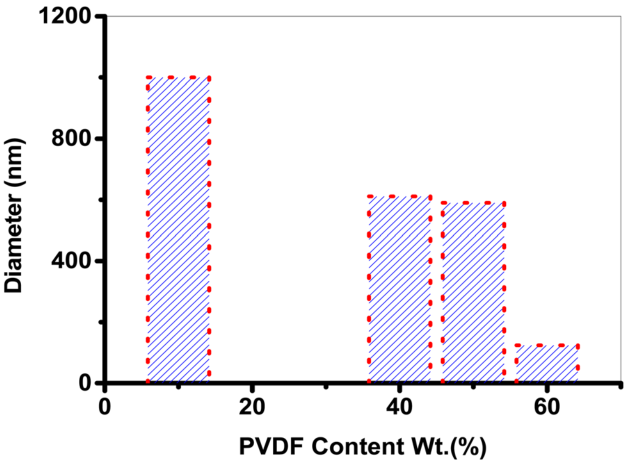

Fig. 17 Correlation between PVDF content and average fiber diameter. Increasing PVDF content from 10% to 60% results in a significant reduction in fiber diameter, reaching a minimum value at the 60 : 40 PVDF : PS composition.

peaks in the spectral range of 3338.5–3650 cm^{-1} could be attributed to crystalline water or the acidic OH groups of carboxylic acids. It can also be obtained from Fig. 21 that most absorption peaks of PVDF, PS and Cu MOF reversed in blended Cu MOF@PVDF–PS membrane.

3.5. X-ray diffraction pattern (XRD)

The XRD pattern of Cu-MOF is shown in Fig. 22. The primary characteristic peaks of Cu-MOF appear at 2θ values of 9.35°, 12°, 16.3°, 17.74°, 20°, and 25.46°, which closely match the simulated pattern.[33,34] The XRD patterns of prepared samples these peaks closely resemble those of the as-synthesized Cu MOF sample, indicating that the good preparation of Cu MOF@PVDF–PS with different concentration as shown in Fig. 23.

3.6. Water uptake and swelling ratio

Since the pristine PVDF/PS membrane is not inherently proton-conductive, water uptake and swelling ratio were primarily evaluated after Cu-MOF incorporation, where hydration plays

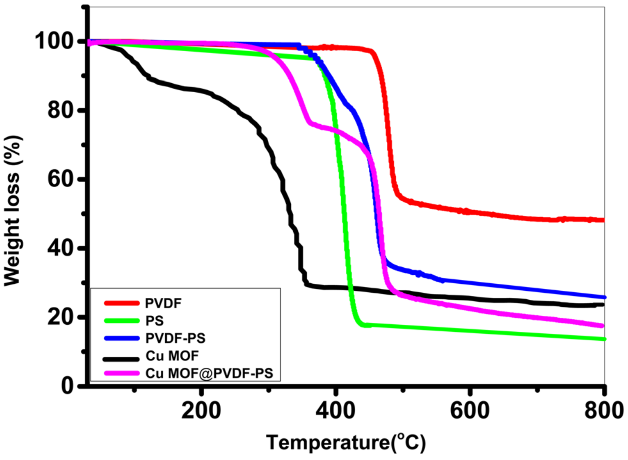

Fig. 18 Thermal stability of Cu MOF, PVDF, PS, PVDF–PS blend nanofiber membranes and Cu MOF (50 wt%)@PS-PVDF.

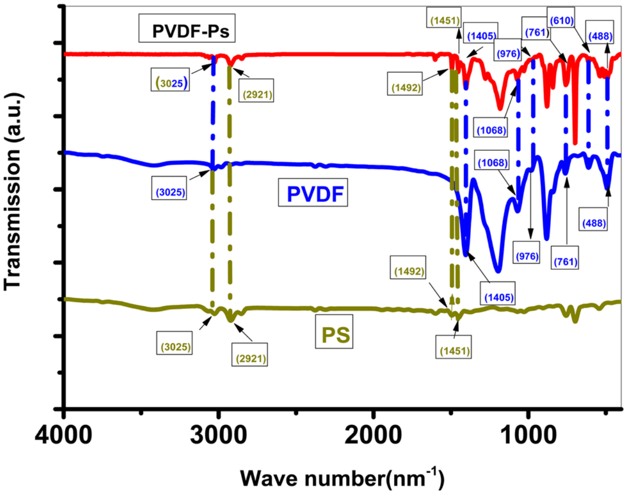

Fig. 19 FTIR spectra pure PS, PVDF and blended membrane (PVDF–PS).

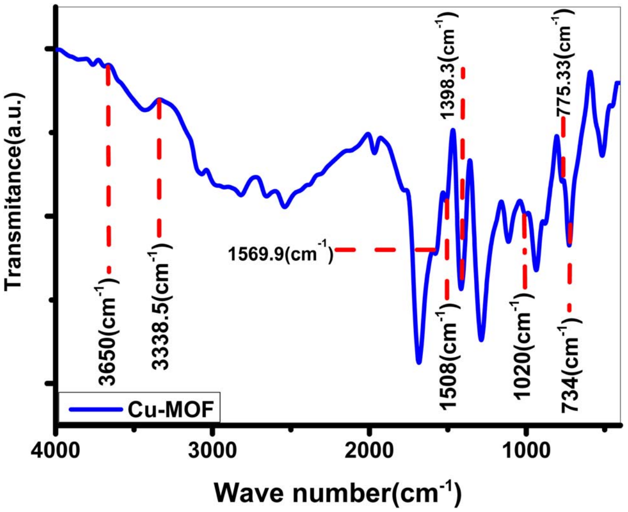

Fig. 20 FTIR spectra of Cu metal organic framework.

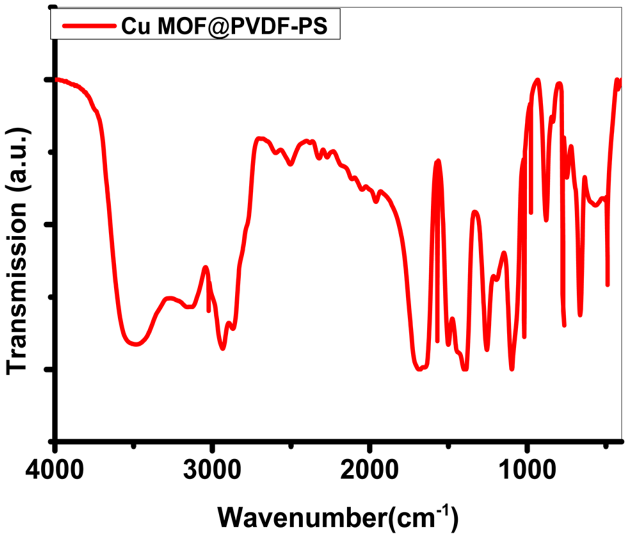

Fig. 21 FTIR spectra pure of blended membrane Cu MOF (50 wt%) @PVDF–PS.

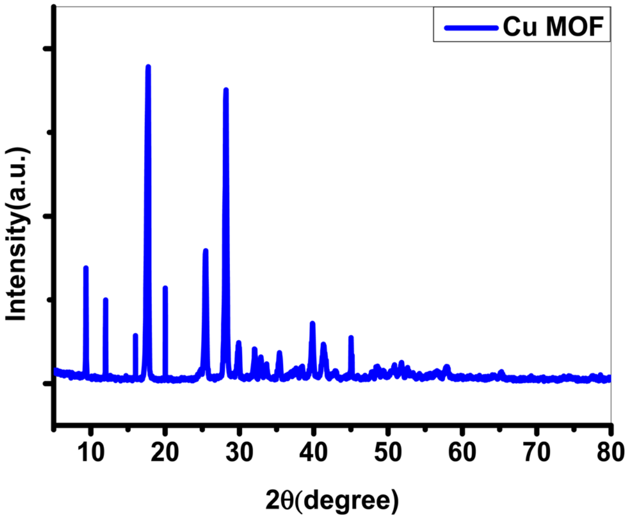

Fig. 22 X-ray diffraction pattern of Cu-MOF metal organic frameworks.

a direct role in enabling and sustaining proton transport. The proton conductivity of membranes is primarily influenced by water uptake and swelling ratio, with the wetting of the PEM affecting proton conductivity and, consequently, fuel cell performance. Therefore, the water uptake and swelling ratio of the as-prepared polyelectrolyte membranes were assessed, and the results are presented in Fig. 24 and 25, respectively. The findings indicate that combining PVDF–PS with Cu MOF increases the water uptake of the resulting blend-based membranes. Moreover, the water absorption increased as the Cu MOF content in the blends was raised. Membranes with a 5 wt% Cu MOF ratio exhibited lower water absorption compared to those with a 50 wt% Cu MOF ratio. This can be explained by the fact that higher concentrations of the

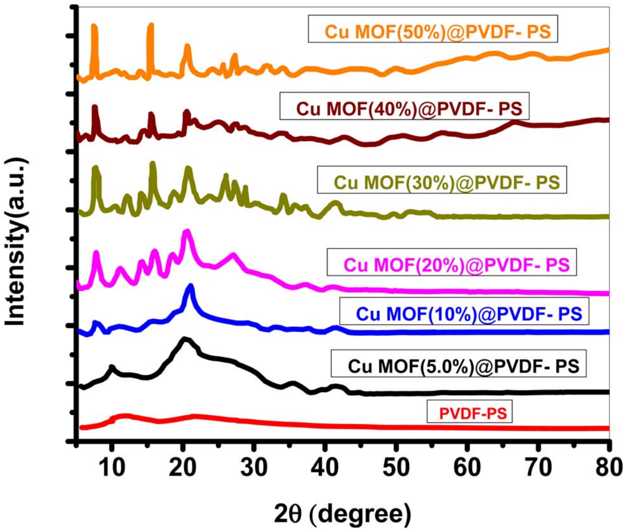

Fig. 23 X-ray diffraction pattern of PVDF–PS, Cu MOF (5 wt%)@PVDF–PS, Cu MOF (10 wt%)@PVDF–PS, Cu MOF (20 wt%)@PVDF–PS, Cu MOF (30 wt%)@PVDF–PS, Cu MOF (40 wt%)@PVDF–PS and Cu MOF (50 wt%)@PVDF–PS.

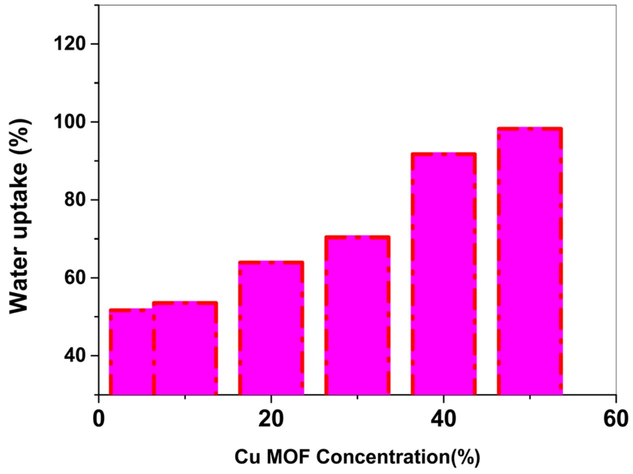

Fig. 24 The water uptake of PVDF–PS@CuMOF membranes with different concentrations of Cu MOF.

conducting material (Cu MOF) increase the availability of hydrophilic groups, thereby enhancing the water absorption capacity of the polyelectrolyte membranes. This observation suggests that Cu MOF has a greater impact than the pure PVDF–PS polymer matrix in improving the water retention of the membranes.[35] IEC and contact angle measurements showed a significant relationship between the quantity of hydrophilic groups in the polymer matrices and the water retention capacity of the membranes. The swelling ratio of the produced polyelectrolyte membranes is determined by the equilibrium between osmotic forces and other dispersive forces. Osmotic forces draw water into the polymer network, while the dispersive forces from the polymer chains resist this movement.[35] The Cu MOF (5 wt%)@PVDF–PS blend membranes exhibited lower swelling values compared to the Cu MOF (50 wt%)@PVDF–PS membranes. The differences in swelling between these membranes are directly related to their water uptake. Greater swelling in polyelectrolyte membranes has been associated with a more hydrophilic membrane surface, which results from the high density of hydrophilic groups.[36] All modified polyelectrolyte membranes exhibit an optimal swelling ratio, as excessive swelling could cause membrane degradation process in water, which is undesirable for membranes used in PEMFC applications. Since water is generated on the cathode side of the fuel cell and the membrane remains in constant contact with it, the fuel cell membrane must be stable in water. The function of the membrane is lost upon dissolution in water. In the event that membranes are soluble in water, this solubility should be as low as is practical.

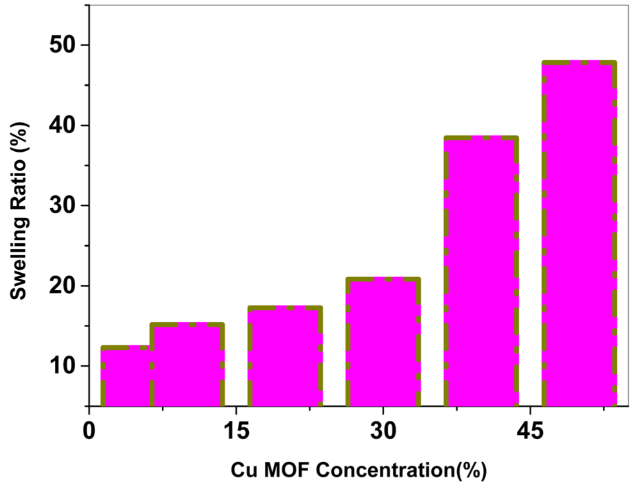

Fig. 25 Swelling ratio measurements of the prepared Cu MOF@PVDF–PS membranes.

3.7. Ion exchange capacity (IEC)

IEC is a dependable and indirect indicator of proton conductivity because it takes into account exchangeable protons within

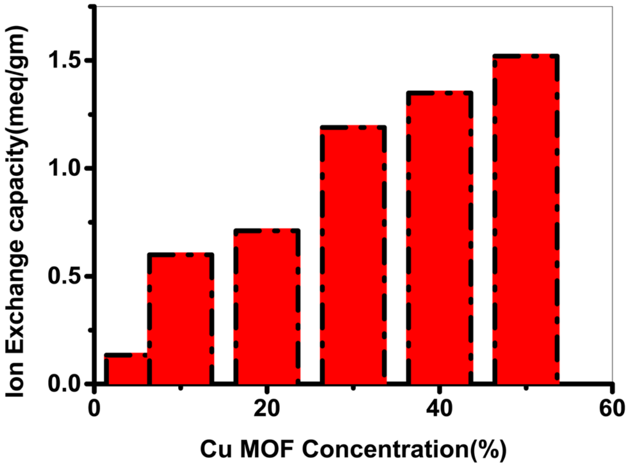

Fig. 26 IEC of Cu MOF@PVDF–PS membranes with varying MOF concentrations.

a polymer matrix, which manages the retention and movement of protons essential for proton conduction from the anode to the cathode. IEC measurements of polymer electrolyte membranes that are made are shown in Fig. 26. As the Cu MOF molar ratio in the membranes rose, the IEC value of PVDF–PS polyelectrolyte membranes increased significantly, going from 0.134 meq g^{-1} for (5% Cu MOF) to 1.52 meq g^{-1} for (50% Cu MOF). By raising the Cu MOF on PVDF–PS based membranes, Leading to a large number of reactive and exchangeable sites in the polymer matrix, this behavior may be shown.[37]

Although increased Cu-MOF content leads to higher water uptake and mechanical flexibility, these effects are beneficial within a controlled range, as they improve proton transport and mechanical compliance. The membrane with 50 wt% Cu-MOF showed a balanced performance with high IEC and proton conductivity, without compromising structural stability, indicating its suitability for fuel cell applications. Additionally, the increased membranes' protonic conductivity values and IEC much improved, especially when mixed polymers filled in the grain boundaries, which greatly facilitated the proton-transferred channel inside the hydrogen-bonding network. Still, they remained higher than Nafion 117 (0.91 meq g^{-1}).[38] The MOF content and nanofiber nature, which changed the electrochemical characteristics of membranes, were blamed for the discrepancies in IEC results. This can be attributed to the fact that IEC and ionic conductivity of fully hydrated Cu MOF@PVDF–PS membranes increased in tandem with the growth of the acid content.

3.8. Methanol uptake (%)

Methanol uptake is another essential measurement that gives a deeper understanding of methanol permeability of the membrane. Typically, membranes with higher methanol uptake values are more permeable to methanol. Fig. 27 illustrates the correlation between methanol uptake and IEC (meq g^{-1}) for the Cu MOF@PVDF–PS membranes. Generally, methanol uptake values were lower than water uptake values, which may be due to the Cu MOF@PVDF–PS membrane being nearly insoluble in methanol,[39,40] which ultimately means that methanol has no direct impact on the Cu MOF@PVDF–PS swelling or viscosity. The sulfonated portion of the membrane is responsible for the

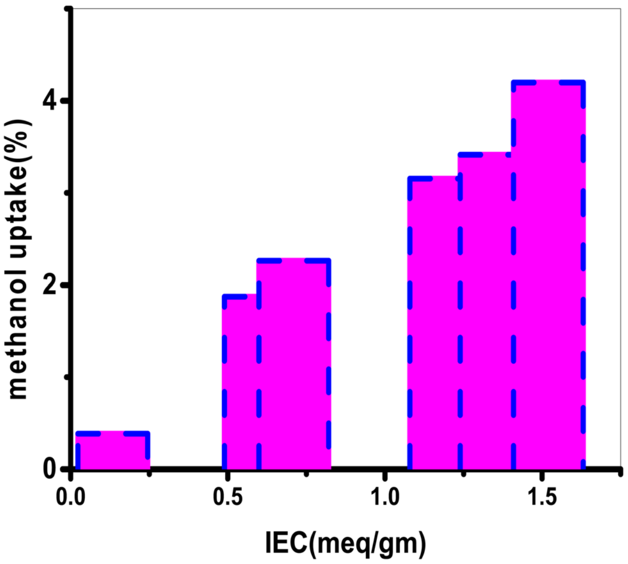

Fig. 27 Methanol uptake (%) as a function of ion-exchange capacity (IEC) (meq g^{-1}) at ambient temperature.

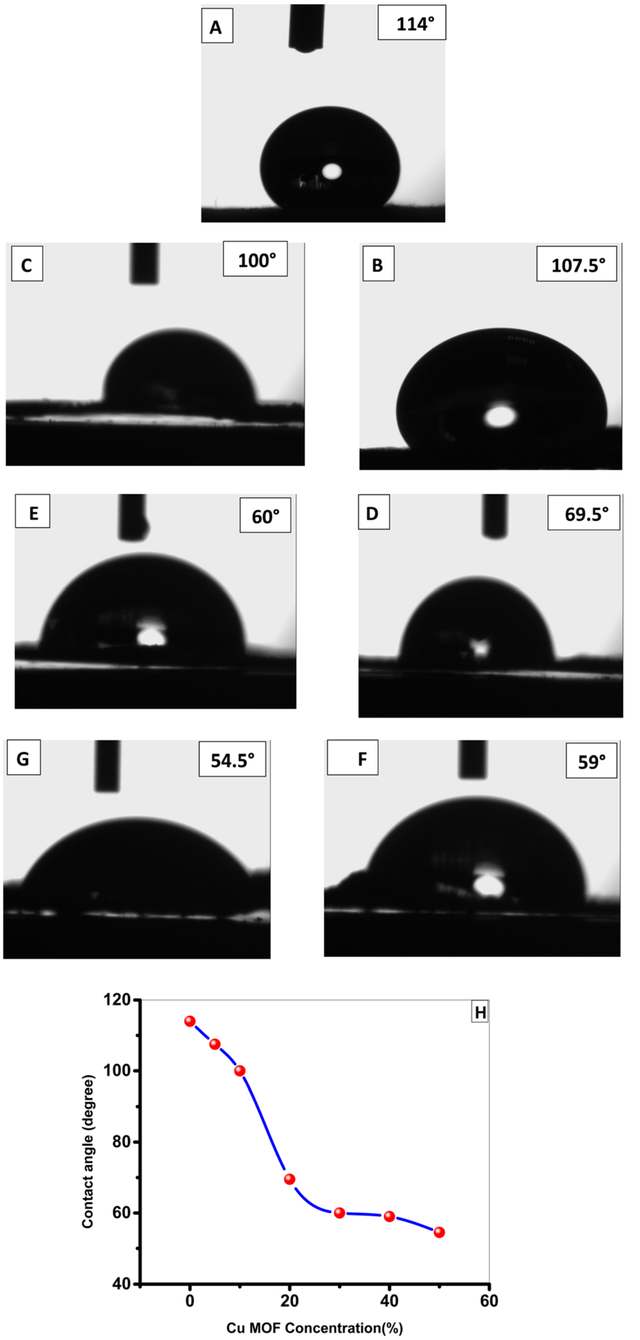

Fig. 28 Contact angle measurements of Cu-MOF@PVDF–PS composite membranes with varying Cu-MOF content (0–50 wt%), (A) 0 wt% Cu-MOF (pristine PVDF–PS), (B) 5 wt% Cu-MOF, (C) 10 wt% Cu-MOF, (D) 20 wt% Cu-MOF, (E) 30 wt% Cu-MOF, (F) 40 wt% Cu-MOF, (G) 50 wt% Cu-MOF and (H) effect of Cu-MOF concentration on the contact angle of PVDF–PS composite membranes.

methanol uptake, which progressively increases as the membrane's IEC rises. The observed increase in methanol uptake with higher IEC values can be attributed to the greater concentration of hydrophilic functional groups introduced by Cu-MOFs. These sites, which are essential for proton conduction, also interact with polar methanol molecules due to their affinity for hydrogen bonding and electrostatic interactions, thereby enhancing methanol absorption within the membrane matrix.

3.9. Contact angle measurements

The wettability behavior of Cu-MOF@PVDF–PS composite membranes was evaluated using static water contact angle measurements, as depicted in Fig. 28. This figure provides a comprehensive visualization of surface hydrophilicity changes across varying Cu-MOF loadings. Fig. 28A shows the pristine PVDF-PS membrane (0 wt% Cu-MOF), exhibiting a high contact angle of 114°, which reflects the inherently hydrophobic nature of the polymer matrix due to the non-polar characteristics of both PVDF and PS.

Upon the addition of Cu-MOF, a gradual reduction in contact angle is observed, indicating enhanced hydrophilicity. As shown in Fig. 28B, the membrane with 5 wt% Cu-MOF displays a contact angle of 107.5°, signifying the onset of improved water affinity. This trend continues with Fig. 28C, where the contact angle decreases to 100° at 10 wt% Cu-MOF. A more pronounced improvement occurs at 20 wt% Cu-MOF (Fig. 28D), with the contact angle significantly reduced to 69.5°, suggesting a threshold level where Cu-MOF begins to uniformly modify the membrane surface.[41,42] At higher loadings, further enhancements in surface wettability are evident. Fig. 28E (30 wt%) shows a contact angle of 60°, while Fig. 28F (40 wt%) indicates a slight decrease to 59°, highlighting the continued benefit of increased Cu-MOF incorporation. The most hydrophilic surface is observed in Fig. 28G at 50 wt% Cu-MOF, where the contact angle drops to 54.5°, confirming optimal surface interaction with water. This progressive shift from hydrophobic to hydrophilic behavior is quantitatively summarized in the plotted trend shown in Fig. 28H, which correlates the decrease in contact angle with increasing Cu-MOF concentration. The enhanced hydrophilicity observed is attributed to the intrinsic

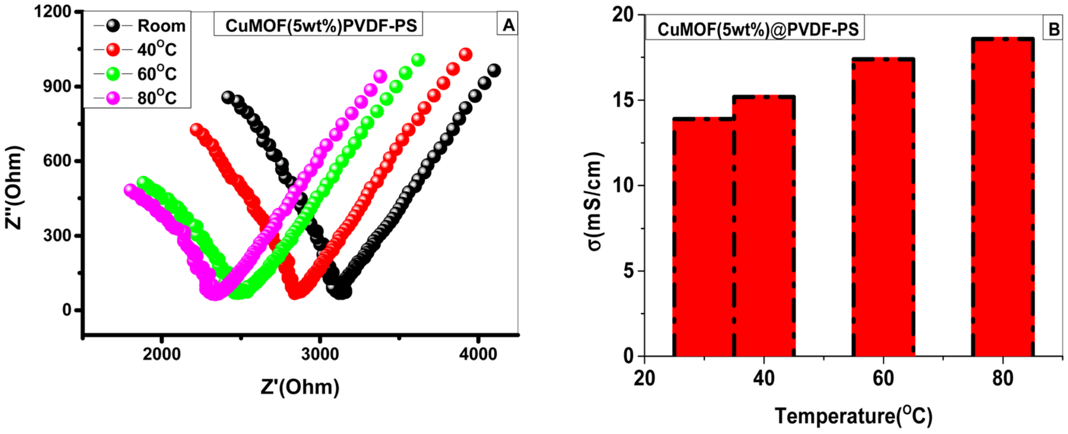

Fig. 29 (A) Nyquist plots of Cu-MOF (5 wt%)@PVDF–PS and (B) the relation between proton conductivity with temperature.

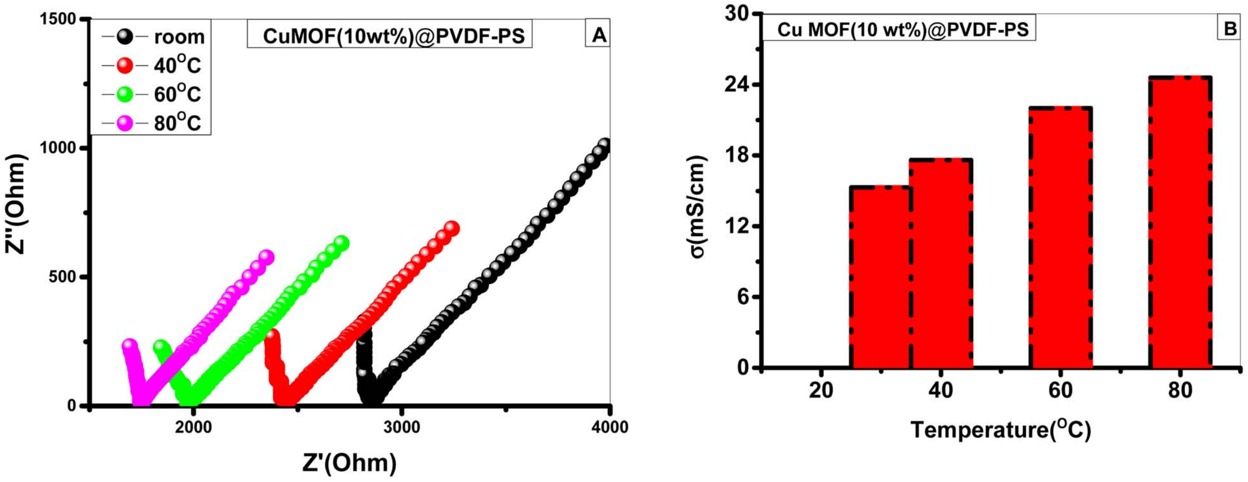

Fig. 30 (A) Nyquist plots of Cu-MOF (10 wt%)@PVDF–PS and (B) the relation between proton conductivity with temperature.

properties of the Cu-MOF particles, which possess polar functional groups and metal coordination sites capable of forming hydrogen bonds with water molecules. These structural features not only improve surface wettability but also support efficient water absorption and continuous hydration both critical for maintaining high proton conductivity in fuel cell membranes.

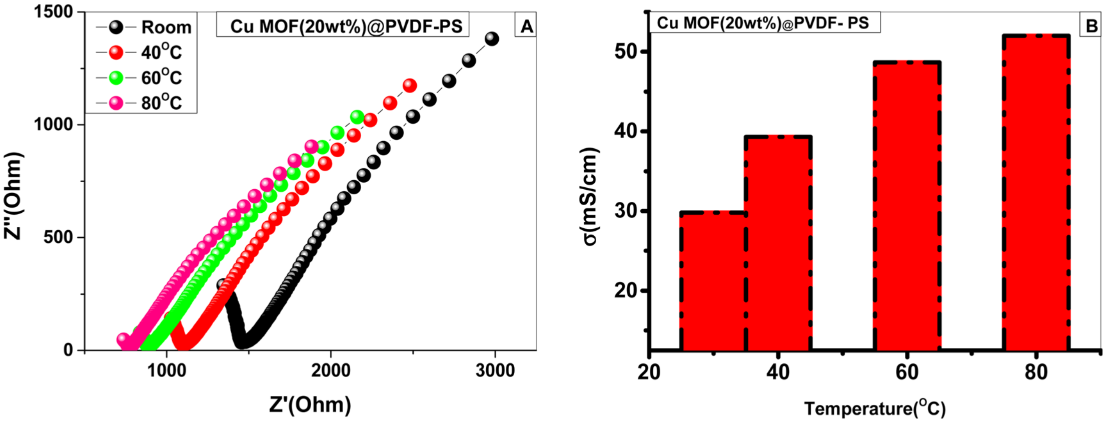

Fig. 31 (A) Nyquist plots of Cu-MOF (20 wt%)@PVDF–PS and (B) the relation between proton conductivity with temperature.

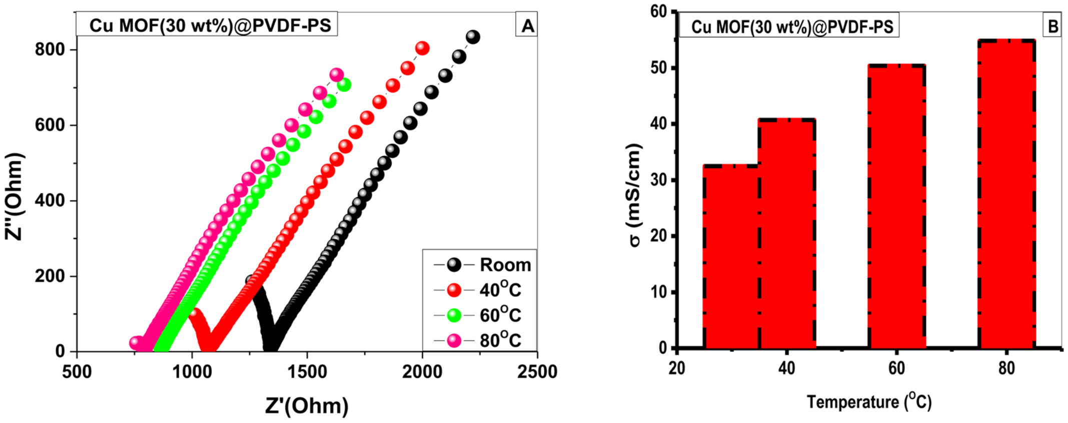

Fig. 32 (A) Nyquist plots of Cu-MOF (30 wt%)@PVDF–PS and (B) the relation between proton conductivity with temperature.

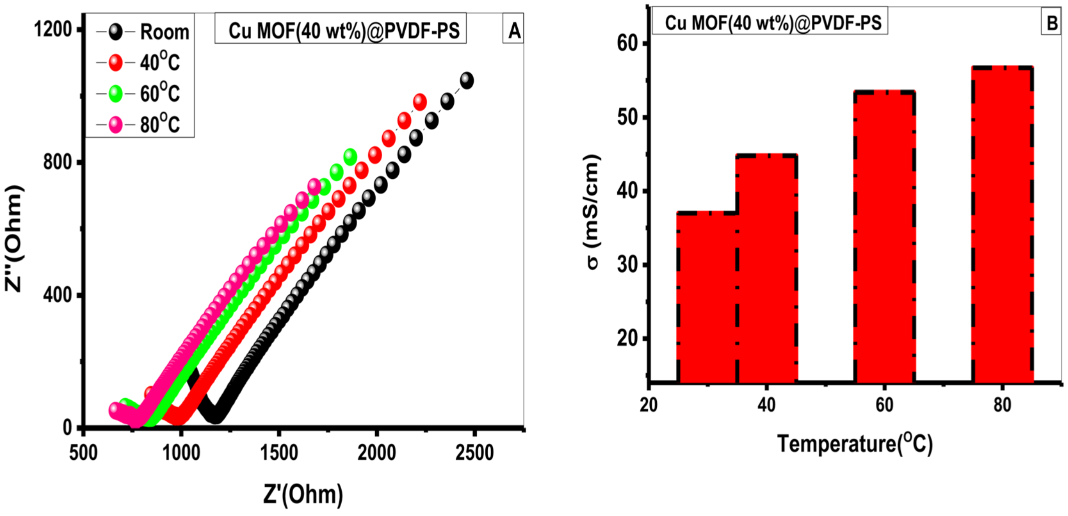

Fig. 33 (A) Nyquist plots of Cu-MOF (40 wt%)@PVDF–PS and (B) the relation between proton conductivity with temperature.

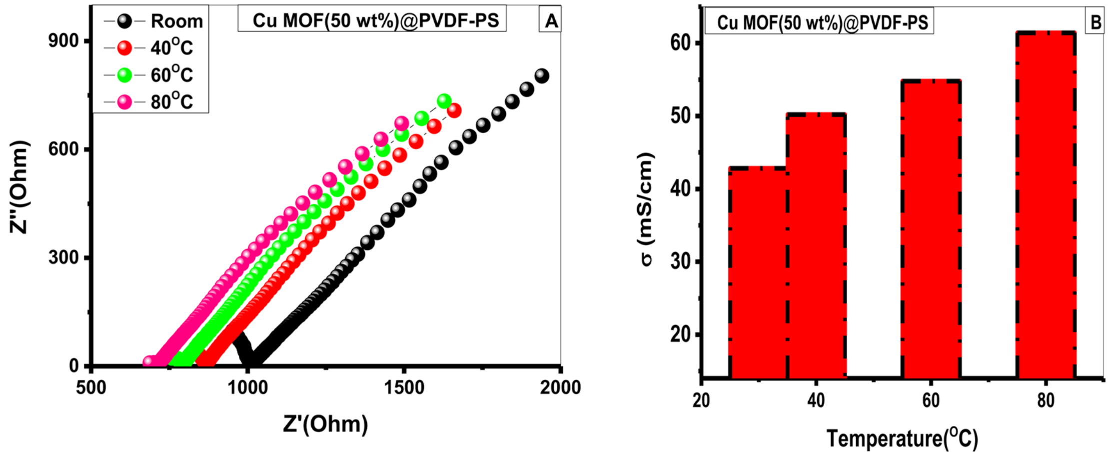

Fig. 34 (A) Nyquist plots of Cu-MOF (50 wt%)@PVDF–PS and (B) the relation between proton conductivity with temperature.

In conclusion, the results from Fig. 28 demonstrate a clear transformation in membrane surface behavior with increasing Cu-MOF content. The shift from a hydrophobic to a highly hydrophilic surface strongly supports the role of Cu-MOF in enhancing membrane performance, making these composite materials excellent candidates for use in proton exchange membrane (PEM) and direct methanol fuel cell (DMFC) systems.

3.10. Proton conductivity of Cu-MOF@nanofiber composite membranes

Impedance spectra were used to evaluate the proton conductivity of the composite membranes Cu-MOF@PVDF–PS. The measurement was conducted using the membranes at temperatures between 30 and 80 °C. As shown in Fig. 29–35, the Nyquist plots of the membranes demonstrate a rise in proton conductivity with rising temperature. The improvements in proton conductivity from 30 to 80 °C are 13.9 to 18.58 mS cm^{-1}, 15.3 to 24.6 mS cm^{-1}, 29.8 to 52 mS cm^{-1}, 32.5 to 54.8 mS cm^{-1}, 37 to 56.7 mS cm^{-1}, 42.8 to 61.4 mS cm^{-1} for Cu MOF (5 wt%)@PVDF–PS, Cu MOF (10 wt%)@PVDF–PS, Cu MOF (20 wt%)@PVDF–PS, Cu MOF (30 wt%)@PVDF–PS, Cu MOF (40 wt%)@PVDF–PS and Cu MOF (50 wt%)@PVDF–PS, respectively. It is significant to remember that as the weight proportion of Cu-MOF within the base matrix rises, so does the proton conductivity. The proton conductivity of Cu MOF (50 wt%)@PVDF–PS is greater than 1 and 3 several orders of magnitude higher than those of the Cu MOF (5 wt%)@PVDF–PS polymers and Cu-MOF samples subjected to the same conditions Fig. 16. This is explained by the synergistic characteristics of the membrane,

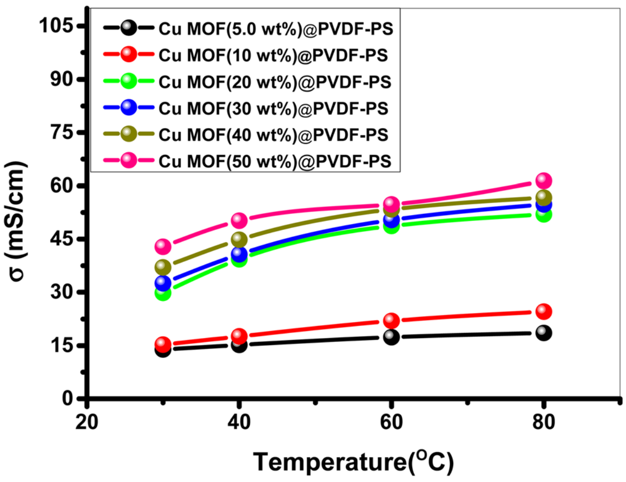

Fig. 35 Variation of proton conductivity (σ) as a function of temperature for Cu-MOF@PVDF-PS composite membranes with different Cu-MOF loadings (5–50 wt%).

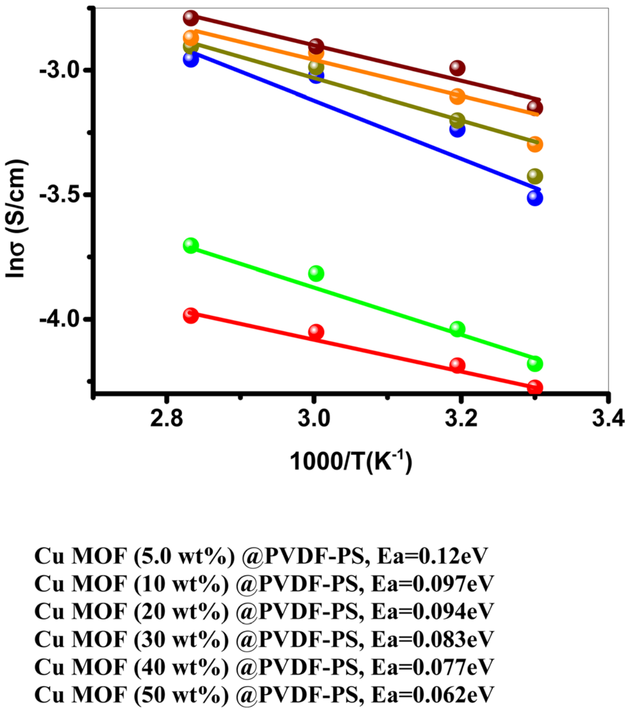

Fig. 36 Arrhenius plots for all of the composite membranes in the temperature range of 30–80 °C.

where the mixed polymers fill in the grain boundaries and greatly facilitate the proton-transferred channel inside. The network of hydrogen bonds. The activation energies were determined to be 0.12, 0.097, 0.094, 0.083, 0.077 and 0.062 eV for Cu MOF (5 wt%)@PVDF–PS, Cu MOF (10 wt%)@PVDF–PS, Cu MOF (20 wt%)@PVDF–PS, Cu MOF (30 wt%)@PVDF–PS, Cu MOF (40 wt%)@PVDF–PS and Cu MOF (50 wt%)@ PVDF–PS, respectively Fig. 36. It appears that the major proton-transferred pathway in all of the composite membranes is a Grotthuss mechanism, as indicated by their lower E_a values (<0.4 eV) to illustrate the Cu-MOF@PVDF–PS composite membrane's resilience, as depicted in Fig. 36.

3.11. BET analysis

The textural properties of the Cu-MOF@PVDF–PS composite membrane were evaluated using nitrogen adsorption–desorption isotherms. The results revealed that the Cu-MOF (50 wt%) @PVDF–PS membrane exhibits a specific surface area of 812 m^2 g^{-1}, a total pore volume of 0.42 cm^3 g^{-1}, and an average pore diameter of 2.1 nm. The isotherm profile corresponds to a type I/IV hybrid with a noticeable hysteresis loop, indicating the presence of both microporous and mesoporous structures. The relatively high surface area is attributed to the well-dispersed Cu-MOF crystals embedded within the nanofibrous PVDF–PS matrix. While the polymer component reduces the overall porosity compared to pure Cu-MOF (1500 m^2 g^{-1}), it provides structural flexibility and processability.[33] The measured pore diameter falls within the optimal range for water adsorption and proton transport, supporting efficient hydration and continuous proton-conductive pathways under fuel cell operating conditions.

These findings confirm that the hybrid membrane structure retains sufficient porosity and accessible surface area, making it a suitable candidate for proton exchange membrane fuel cells (PEMFCs) and direct methanol fuel cells (DMFCs).

3.12. Testing the cell

The Cu-MOF (50 wt%)@PVDF–PS membrane was selected for fuel cell evaluation due to its outstanding properties among the fabricated membranes. It exhibited superior proton conductivity, high ion exchange capacity (IEC), enhanced hydrophilicity, and favorable mechanical characteristics, making it an excellent candidate for practical DMFC applications. These attributes, especially the improved water uptake and mechanical resilience, supported efficient proton conduction and long-term operational stability.

In a direct methanol fuel cell (DMFC), methanol is oxidized at the anode while oxygen is reduced at the cathode, generating electrical current *via* an external circuit. The proton exchange membrane (PEM) serves a dual role: enabling proton transport while limiting methanol crossover. Excessive methanol permeation to the cathode leads to mixed potentials and a drop in open circuit voltage (OCV), ultimately reducing performance. To evaluate the PEM functionality, the Cu-MOF (50 wt%)@PVDF–PS membrane was tested in a DMFC single cell using varying methanol concentrations.

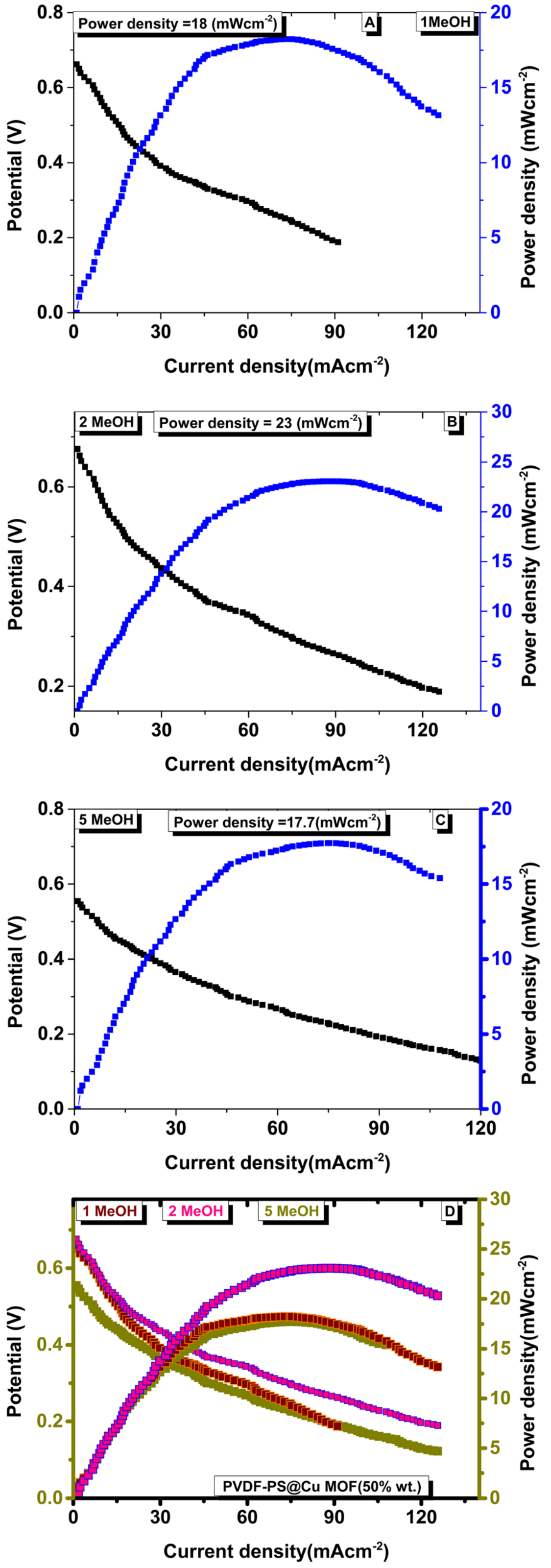

Fig. 37 Electrochemical performance of a direct methanol fuel cell (DMFC) utilizing a Cu-MOF (50 wt%) @PVDF–PS composite membrane under varying methanol concentrations in 1 M H_2SO_4. (A) DMFC performance at 1 M methanol. (B) DMFC performance at 2 M methanol. (C) DMFC performance at 5 M methanol. (D) Polarization and power density curves of a direct methanol fuel cell (DMFC) using a Cu-MOF (50 wt%)@PVDF–PS membrane at different methanol concentrations (1 M, 2 M, and 5 M) in 1 M H_2SO_4.

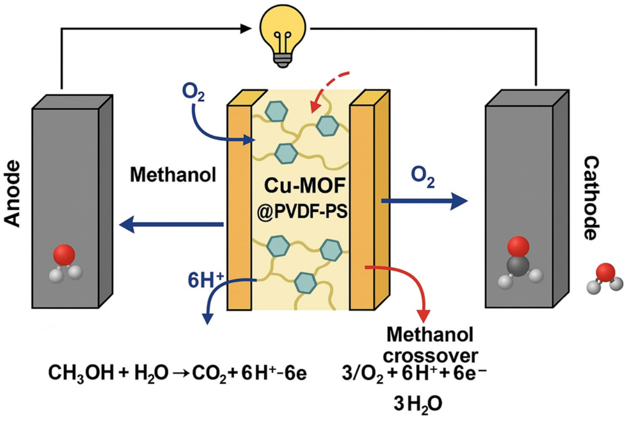

Fig. 38 Schematic representation of proton transport and methanol suppression. A visual diagram of the DMFC setup using the Cu-MOF@PVDF–PS membrane. The image illustrates proton conduction pathways facilitated by the MOF structure and the membrane's role in minimizing methanol permeation, thus enhancing efficiency and maintaining cathodic selectivity.

Fig. 37 illustrates the electrochemical behavior of the DMFC system employing the Cu-MOF-based composite membrane. Fig. 37A presents the fuel cell performance at 1 M methanol, where the power density reached 18 mW cm^{-2}, and the OCV remained stable around 0.65 V. At 2 M methanol (Fig. 37B), a notable enhancement was observed, with a peak power density of 23 mW cm^{-2}, indicating an optimal fuel concentration that balances proton generation and methanol crossover. However, increasing the concentration to 5 M methanol (Fig. 37C) resulted in performance decline; the excessive fuel crossover led to a mixed potential at the cathode, reducing both the OCV to 0.55 V and power density to 17.7 mW cm^{-2}.

These findings are consolidated in Fig. 37D, which displays the polarization and power density curves across all tested methanol concentrations (1 M, 2 M, and 5 M). The composite membrane's performance enhancement is attributed to the uniform dispersion of Cu-MOF particles within the PVDF–PS nanofiber network, which facilitates proton transport via additional conduction pathways and mitigates methanol crossover through its dense structure. This synergy leads to reduced internal resistance and more efficient cathodic reactions, ultimately boosting cell performance.

The results affirm that the Cu-MOF@PVDF–PS membrane achieves a favorable balance between conductivity and methanol suppression, positioning it as a promising PEM material for DMFC systems. A visual representation of the fuel cell operation and internal transport mechanisms supported by the composite membrane is provided in Fig. 38, which highlights proton conduction through Cu-MOF active sites, minimized methanol diffusion, and the overall electrochemical processes governing DMFC functionality.

4. Conclusion

This study investigates the electrospinning process for fabricating PVDF–PS nanofibers, focusing on key process parameters. The effects of high voltage, polymer concentration, and solution flow rate were examined. The optimal conditions for obtaining PVDF–PS nanofibers were determined to be a flow rate of 1 mL h^{-1}, a high voltage of 20 kV, and a polymer concentration of 10 wt%. The fiber diameter was primarily influenced by two key factors: polymer concentration and applied voltage, both of which significantly impacted fiber morphology. Additionally, the PVDF–PS blend nanofiber membrane was studied for use as a high-temperature proton exchange membrane (HT-PEM). Thermogravimetric analysis (TGA) was used to evaluate thermal stability, and FTIR analysis confirmed the preparation of PVDF–PS. After fabrication and analysis, the single-fiber PVDF–PS membranes were assessed for potential use in PEM fuel cells. Well-formed electrospun nanofiber mats, specifically with a PVDF60–PS40 weight ratio, were produced. These mats were then hot-pressed and thermally annealed to form dense, defect-free membranes, preserving the nanomorphology of PVDF–PS fibers.

Furthermore, a series of composite membranes incorporating Cu-MOF@PVDF–PS matrix were successfully fabricated. The Cu-MOF (50 wt%)@PVDF–PS composite membrane demonstrated impressive proton conductivity of 61.4 mS cm^{-1} at 353 K, significantly outperforming the pure Cu-MOF@PVDF–PS matrix. The constructive interaction between Cu-MOF and the PVDF–PS matrix is believed to have an essential impact in enhancing the proton-conducting pathway. These findings provide valuable insights for the effective use of MOF/polymer-based materials in proton exchange membranes for electrochemical devices.

Finally, the Cu-MOF (50 wt%)@PVDF–PS composite membrane holds considerable promise as a proton exchange membrane (PEM) for direct methanol fuel cells (DMFCs). It demonstrates strong power density and open circuit voltage (OCV) performance, with a peak power density of 23 mW cm^{-2} at 2 M methanol. The uniform the distribution of Cu-MOF within the PVDF–PS matrix enhances ion transport, reduces cell resistance, and enhances the overall efficiency of the cell. While performance slightly decreases at higher methanol concentrations, this composite membrane remains a promising candidate for DMFC applications.

Conflicts of interest

There are no conflicts to declare.

Data availability

The datasets generated during the current study are available from the corresponding author on reasonable request.

Acknowledgements

This work is supported by the Science, Technology & Innovation Funding Authority (STDF) under the grant (YRG Call 10), project ID (43211).

References

1 A. B. Stambouli and E. Traversa, Fuel cells, an alternative to standard sources of energy, *Renewable Sustainable Energy Rev.*, 2002, **6**(3), 295–304.
2 K.-D. Kreuer, S. J. Paddison, E. Spohr and M. Schuster, Transport in proton conductors for fuel-cell applications: simulations, elementary reactions, and phenomenology, *Chem. Rev.*, 2004, **104**(10), 4637–4678.
3 X. Wen, Q. Zhang and J. Guan, Applications of metal–organic framework-derived materials in fuel cells and metal-air batteries, *Coord. Chem. Rev.*, 2020, **409**, 213214.
4 D. W. Kang, M. Kang and C. S. Hong, Post-synthetic modification of porous materials: superprotonic conductivities and membrane applications in fuel cells, *J. Mater. Chem. A*, 2020, **8**(16), 7474–7494.
5 H. Zhang and P. K. Shen, Recent development of polymer electrolyte membranes for fuel cells, *Chem. Rev.*, 2012, **112**(5), 2780–2832.
6 A. Shigematsu, T. Yamada and H. Kitagawa, Wide control of proton conductivity in porous coordination polymers, *J. Am. Chem. Soc.*, 2011, **133**(7), 2034–2036.
7 K.-D. Kreuer, Proton conductivity: materials and applications, *Chem. Mater.*, 1996, **8**(3), 610–641.
8 K. A. Mauritz and R. B. Moore, State of Understanding of Nafion, *Chem. Rev.*, 2004, **104**(10), 4535–4586.
9 K.-D. Kreuer, Proton Conductivity: Materials and Applications, *Chem. Mater.*, 1996, **8**(3), 610–641.
10 T. D. Gierke, G. Munn and F. Wilson, The morphology in Nafion perfluorinated membrane products, as determined by wide-and small-angle X-ray studies, *J. Polym. Sci. Polym. Phys. Ed.*, 1981, **19**(11), 1687–1704.
11 S. Ivanchev, Fluorinated proton-conduction Nafion-type membranes, the past and the future, *Russ. J. Appl. Chem.*, 2008, **81**, 569–584.
12 G. K. Shimizu, J. M. Taylor and S. Kim, Proton conduction with metal–organic frameworks, *Science*, 2013, **341**(6144), 354–355.
13 A.-L. Li, Q. Gao, J. Xu and X.-H. Bu, Proton-conductive metal–organic frameworks: recent advances and perspectives, *Coord. Chem. Rev.*, 2017, **344**, 54–82.
14 P. Ramaswamy, N. E. Wong and G. K. Shimizu, MOFs as proton conductors–challenges and opportunities, *Chem. Soc. Rev.*, 2014, **43**(16), 5913–5932.
15 F. Yang, G. Xu, Y. Dou, B. Wang, H. Zhang, H. Wu, *et al.*, A flexible metal–organic framework with a high density of sulfonic acid sites for proton conduction, *Nat. Energy*, 2017, **2**(11), 877–883.
16 G. E. Wang, G. Xu, B. W. Liu, M. S. Wang, M. S. Yao and G. C. Guo, Semiconductive nanotube array constructed from giant $[\mathrm{Pb^{II}}_{18}\mathrm{I}_{54}(\mathrm{I}_2)_9]$ wheel clusters, *Angew. Chem.*, 2016, **128**(2), 524–528.
17 X.-N. Zou, D. Zhang, Y. Xie, T.-X. Luan, W. Li, L. Li, *et al.*, High enhancement in proton conductivity by incorporating sulfonic acids into a zirconium-based metal–organic framework *via* "click" reaction, *Inorg. Chem.*, 2021, **60**(14), 10089–10094.
18 X.-Y. Dong, J.-J. Li, Z. Han, P.-G. Duan, L.-K. Li and S.-Q. Zang, Tuning the functional substituent group and guest of metal–organic frameworks in hybrid membranes for improved interface compatibility and proton conduction, *J. Mater. Chem. A*, 2017, **5**(7), 3464–3474.
19 X. Liang, F. Zhang, W. Feng, X. Zou, C. Zhao, H. Na, *et al.*, From metal–organic framework (MOF) to MOF–polymer composite membrane: enhancement of low-humidity proton conductivity, *Chem. Sci.*, 2013, **4**(3), 983–992.
20 K. Cai, F. Sun, X. Liang, C. Liu, N. Zhao, X. Zou, *et al.*, An acid-stable hexaphosphate ester based metal–organic framework and its polymer composite as proton exchange membrane, *J. Mater. Chem. A*, 2017, **5**(25), 12943–12950.
21 X. Xu, H. Wang, S. Lu, S. Peng and Y. Xiang, A phosphotungstic acid self-anchored hybrid proton exchange membrane for direct methanol fuel cells, *RSC Adv.*, 2016, **6**(49), 43049–43055.
22 R. Moi, A. Ghorai, S. Banerjee and K. Biradha, Amino-and sulfonate-functionalized metal–organic framework for fabrication of proton exchange membranes with improved proton conductivity, *Cryst. Growth Des.*, 2020, **20**(8), 5557–5563.
23 S. Zhang, G. He, X. Gong, X. Zhu, X. Wu, X. Sun, *et al.*, Electrospun nanofiber enhanced sulfonated poly(phthalazinone ether sulfone ketone) composite proton exchange membranes, *J. Membr. Sci.*, 2015, **493**, 58–65.
24 H.-Y. Li and Y.-L. Liu, Polyelectrolyte composite membranes of polybenzimidazole and crosslinked polybenzimidazole-polybenzoxazine electrospun nanofibers for proton exchange membrane fuel cells, *J. Mater. Chem. A*, 2013, **1**(4), 1171–1178.
25 P. Kallem, N. Yanar and H. Choi, Nanofiber-based proton exchange membranes: development of aligned electrospun nanofibers for polymer electrolyte fuel cell applications, *ACS Sustain. Chem. Eng.*, 2018, **7**(2), 1808–1825.
26 Q. Yuan, Z. Fu, Y. Wang, W. Chen, X. Wu, X. Gong, *et al.*, Coaxial electrospun sulfonated poly(ether ether ketone) proton exchange membrane for conductivity-strength balance, *J. Membr. Sci.*, 2020, **595**, 117516.
27 Y.-l Lei, Y.-j Luo, F. Chen and L.-h Mei, Sulfonation process and desalination effect of polystyrene/PVDF semi-interpenetrating polymer network cation exchange membrane, *Polymers*, 2014, **6**(7), 1914–1928.
28 G. Gallagher, R. Jakeways and I. Ward, The structure and properties of drawn blends of poly(vinylidene fluoride) and poly(methyl methacrylate), *J. Polym. Sci., Part B:Polym. Phys.*, 1991, **29**(9), 1147–1162.
29 S.-H. Hong, S.-A. Lee, J.-D. Nam, Y.-K. Lee, T.-S. Kim and S. Won, Platinum-catalyzed and ion-selective polystyrene fibrous membrane by electrospinning and *in situ* metallization techniques, *Macromol. Res.*, 2008, **16**, 204–211.
30 Effect of annealing process on the phase formation in poly(vinylidene fluoride) thin films, *AIP Conference*

Proceedings, ed. I. Y. Abdullah, M. Yahaya, M. H. H. Jumali and H. M. Shanshool, American Institute of Physics, 2014.

31 S. Rostamnia and Z. Karimi, Preparation and catalytically study of metal–organic frameworks of amine/MIL-53 (Al) as a powerful option in the rapid N-formylation condensation in neat conditions, *Inorg. Chim. Acta*, 2015, **428**, 133–137.

32 S. Rostamnia and A. Morsali, Size-controlled crystalline basic nanoporous coordination polymers of Zn_4O (H_2N-TA)$_3$: catalytically study of IRMOF-3 as a suitable and green catalyst for selective synthesis of tetrahydro-chromenes, *Inorg. Chim. Acta*, 2014, **411**, 113–118.

33 C. G. Carson, K. Hardcastle, J. Schwartz, X. Liu, C. Hoffmann and R. A. Gerhardt, *et al.*, *Synthesis and Structure Characterization of Copper Terephthalate Metal–Organic Frameworks*, Wiley Online Library, 2009.

34 S. L. Rodríguez, G. A. Ortega-Moreno, M. Sánchez-Sánchez, J. L. Fernández and J. M. Zamaro, Structural Transition in the Growth of Copper Terephthalate Metal–Organic Frameworks: Understanding the Effect of the Synthetic Protocol and Its Impact on Electrochemical Behavior, *Coatings*, 2023, **13**(12), 2065.

35 M. M. Eldin, A. Elzatahry, K. El-Khatib, E. Hassan, M. El-Sabbah and M. Abu-Saied, Novel grafted Nafion membranes for proton-exchange membrane fuel cell applications, *J. Appl. Polym. Sci.*, 2011, **119**(1), 120–133.

36 J. Reyes-Rodriguez, O. Solorza-Feria, A. García-Bernabé, E. Giménez, O. Sahuquillo and V. Compañ, Conductivity of composite membrane-based poly(ether-ether-ketone) sulfonated (SPEEK) nanofiber mats of varying thickness, *RSC Adv.*, 2016, **6**(62), 56986–56999.

37 H. Nagar, N. Sahu, V. B. Rao and S. Sridhar, Surface modification of sulfonated polyethersulfone membrane with polyaniline nanoparticles for application in direct methanol fuel cell, *Renewable Energy*, 2020, **146**, 1262–1277.

38 S. Awad, A. H. Alomari, E. E. Abdel-Hady and M. F. Hamam, Characterization, nanostructure, and transport properties of styrene grafted PVA/SiO_2 hybrid nanocomposite membranes: positron lifetime study, *Polym. Adv. Technol.*, 2021, **32**(4), 1742–1751.

39 A. Kraytsberg and Y. Ein-Eli, Review of advanced materials for proton exchange membrane fuel cells, *Energy Fuels*, 2014, **28**(12), 7303–7330.

40 E. Abdel-Hady, M. Abdel-Hamed, S. Awad and M. Hmamm, Characterization and evaluation of commercial poly(vinylidene fluoride)-*g*-sulfonated polystyrene as proton exchange membrane, *Polym. Adv. Technol.*, 2018, **29**(1), 130–142.

41 Y. Cui, Y. Yue, G. Qian and B. Chen, Luminescent functional metal–organic frameworks, *Chem. Rev.*, 2012, **112**(2), 1126–1162.

42 Z. Hasan and S. H. Jhung, Removal of hazardous organics from water using metal-organic frameworks (MOFs): plausible mechanisms for selective adsorptions, *J. Hazard. Mater.*, 2015, **283**, 329–339.